# Transonic Lift and Drag Predictions using Wall Modelled Large Eddy Simulations

Aditya S. Ghate[*], Gaetan K. Kenway[†], Gerrit-Daniel Stich[‡],
Oliver M. F. Browne[§], Jeffrey A. Housman[¶], and Cetin C. Kiris[‖]
*NASA Ames Research Center, Moffett Field, CA 94035*

**Wall-modelled Large Eddy Simulations (WMLES) of the NASA Common Research Model (CRM) at transonic conditions and various angles of attacks leading up to and including shock-induced flow separation are performed using the LAVA computational framework. The simulations are shown to accurately predict the lift curve slope and the onset of separation characterized by the break in the pitching moment. Furthermore, careful assessment of skin-friction drag at cruise condition and its subsequent decrease with increasing angles of attack are shown to be in agreement with viscous sublayer resolving Reynolds Averaged Navier Stokes (RANS) simulations. The small differences between WMLES and RANS appear to be of the same order as differences seen between two RANS models at the cruise-point. Some sensitivity is observed to the coefficient used in the subgrid scale model, although this can be reconciled by noting the low chord- and shock-incidence Reynolds numbers ($\mathrm{Re}_x \approx 10^6$) seen in the outboard regions of the wing, along with the uncertainties associated with tripping and the numerical transition that occurs near the leading edge. Among the primary drawbacks seen in the WMLES predictions is the subdued increase in wave-drag with increasing angle-of-attack and the shock intensity when compared with experimental data. Preliminary assessment suggests that additional span- and stream-wise grid resolution is likely needed in mid- and out-board portions of the wing to better resolve the shock-induced separated flow and to further investigate prediction accuracy of unsteady temporal characteristics of the problem.**

## I. Introduction

Computational Fluid Dynamics (CFD) using Reynolds Averaged Navier Stokes (RANS) based closure modeling has become a cornerstone in aircraft aerodynamic analysis, facilitated primarily by the emergence of high-performance computing. While the availability of efficient algorithms for rapid steady-state modeling has resulted in maturity of RANS-based multi-disciplinary design optimization (MDO) over the last two decades [1–6], the vast majority of such efforts has focused on operating conditions near the high-speed cruise point which accounts for less than 25% of the total aerodynamics related development effort [7]. As the role of CFD advances beyond design and optimization and towards *Certification and Qualification by Analysis* (CQbA) in an attempt to alleviate the high financial burden of wind tunnel and flight testing, there is growing interest in expanding the scope of high-fidelity numerical modeling to target regions of the flight envelope characterized by large regions of separated flows [8]. A distinguishing feature of separated flows is that the mean (time/ensemble averaged) flow is strongly influenced by the dynamics of large scales (dictated by the geometry scale) of turbulence, and it is now universally acknowledged that the majority of RANS closures, including second moment closures, have very limited success in such flow conditions [9]. Some examples of such failures of RANS in external aerodynamics include smooth-body separation associated with high-lift devices at low-speeds during landing (focus of the high lift prediction workshops) [10] and side-of-body corner flow separation (focus of the juncture flow workshop) [11]. A third example is the flow instability phenomenon involving unsteady shock-boundary layer interactions resulting in self-sustained low-frequency oscillations, commonly referred to as *transonic buffet*. This phenomenon poses a considerable challenge for aircraft maneuverability, limiting the operational flight envelope. Predictive numerical estimation of aerodynamic loading at flow conditions leading up to and including this flow phenomenon is the focus of the present study.

[*]Science and Technology Corporation, AIAA Member, aditya.s.ghate@nasa.gov
[†]Science and Technology Corporation, AIAA Member, gaetan.k.kenway@nasa.gov
[‡]Science and Technology Corporation, AIAA Member, gerrit-daniel.stich@nasa.gov
[§]Science and Technology Corporation, AIAA Member, oliver.m.browne@nasa.gov
[¶]Computational Aerosciences Branch, AIAA Senior Member, jeffrey.a.housman@nasa.gov
[‖]Computational Aerosciences Branch, AIAA Senior Member, cetin.c.kiris@nasa.gov
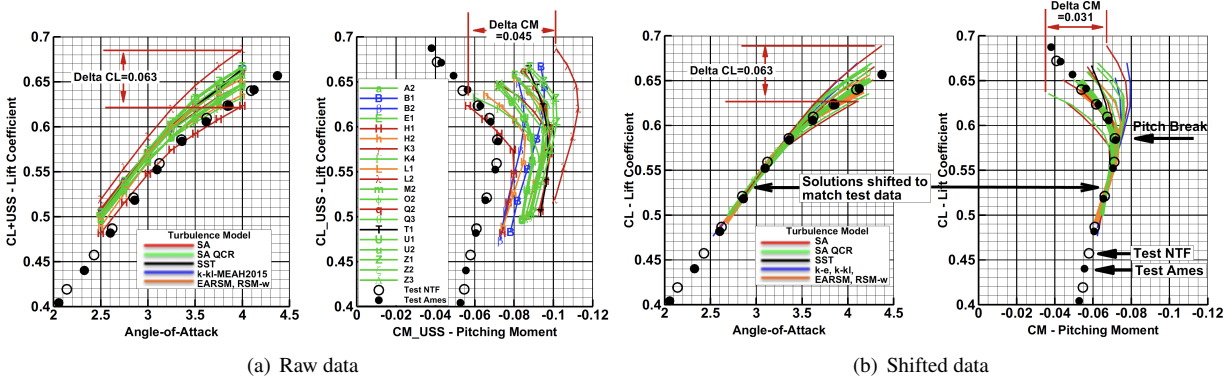
**Fig. 1  RANS predictions from 6th AIAA Drag Prediction Workshop, 2016. Note that the outliers that lacked quadratic corrections such as QCR, predicted spurious side-of-body separation bubbles and have been excluded from the figure. Figure courtesy of Ed Tinoco (AIAA-2020-2745)[7].**

Shock-induced flow separation has been studied extensively using experiments in the context of canonical oblique shock turbulent boundary layer interaction (OSTBLI) problems [12, 13], and two-dimensional airfoils in transonic conditions [14–16]. Many theories involving wave-propagation feedback mechanism [17] and onset of a global instability [18] have been proposed to explain the self-sustaining oscillations. In terms of numerical investigations, perhaps the most comprehensive work on this topic is by Morgan et al. (2013)[19] who study the canonical OSTBLI problem using Large Eddy Simulations and highlight deficiencies of several RANS closures via a systematic Reynolds stress budget analysis. The inaccuracies in modeling turbulent transport terms and isotropic treatment of dissipation are identified as the primary cause of failure even in Reynolds stress-transport models. Scale resolving simulations that explicitly resolve the geometry-influenced large scales of turbulence and model the more universal small-scales are naturally suited to handle high Reynolds number non-equilibrium wall turbulence [20, 21], including that seen in shock induced boundary layer separation. As such the problem of transonic buffet has been studied with canonical two-dimensional airfoils using both hybrid RANS/LES [22–25] and more recently with wall-modelled Large Eddy Simulations (WMLES) [26]. Both simulation methodologies show significant improvements over steady state RANS computations in terms of shock positions quantified using comparisons of pressure distribution with experiments by Jacquin et al. (2009)[16].

Beyond these investigations involving canonical geometries, the Drag Prediction Workshops (1-6) through the past two decades have addressed the accuracy of RANS-based CFD predictions at flow conditions around the cruise-point for full aircraft (tube-and-body) configurations. A summary of RANS predictions from the most recent workshop (DPW6) involving transonic flow conditions on the NASA Common Research Model (CRM) is shown in Figure 1, highlighting the challenges faced by RANS modeling after the onset of shock-induced flow separation. The reader is referred to a comprehensive summary paper by Tinoco (2020)[7] for further details including an important discussion regarding uncertainties associated with experimental measurements used for comparison with free-air numerical simulations.

Simulations reported in this paper were performed using the structured curvilinear overset Navier-Stokes solver within the Launch, Ascent, and Vehicle Aerodynamics (LAVA) computational framework [27]. This framework is currently under active development with a focus on scale resolving simulations for a variety of grid paradigms and turbulence modeling strategies. These include hybrid RANS/LES using structured curvilinear overset meshes [28], and WMLES using both unstructured and structured curvilinear Navier-Stokes formulations [29–31], as well as Cartesian immersed boundary treatment with Navier-Stokes and Lattice Boltzmann algorithms [32, 33].

In the present work, we utilize the geometry used as part of DPW-6 with all simulations performed at a Reynolds number of 5 million (based on the crank chord) and a free-stream Mach number of 0.85. All the wall-modelled Large Eddy Simulations (WMLES) are performed with the aim of addressing the following key questions:

1) Can WMLES be used to accurately predict skin friction drag at cruise conditions?
2) Can WMLES model the progression of shock-induced separation? This involves the predictability of the following two metrics:
    a Accurate lift-curve slope and the pitching moment in the linear regime representing the change in shock location with changes in the angle of attack.
    b Accurate prediction of the *pitch break* representing onset of shock-induced flow separation that occurs at

$C_L \approx 0.6$ ,and accurate prediction of the lift curve slope beyond this point.

3) Can constant/static coefficient subgrid scale modeling be used for external aerodynamics involving predictive simulations of shock-boundary layer interactions?

4) Can WMLES accurately predict the buffet intensity measured using the wing root bending moment seen in experiments by Balakrishna & Acheson (2011)? [34].

5) Can WMLES accurately predict the tonal and broadband character of pressure fluctuations near the trailing edge as seen in experiments of Jacquin et al. (2009)? [[16]].

This paper attempts to address questions 1-3 by systematic analysis using two configurations shown in Figure 2: a) Fixed (un-deformed) wing-only geometry, and b) Wing-body geometry including the static deflections provided in DPW6. Questions 4 and 5 will be the focus of a future paper. The remainder of the paper is outlined as follows. In Section 2, we summarize the wall-treatment (equilibrium wall-model) used in the paper. We also briefly describe the Delayed Detached Eddy Simulation (DDES) algorithm used in one of the wing-only configuration tests to supplement the RANS and WMLES results reported. Section 3 describes the numerical discretization including the shock-sensor used to localize numerical dissipation for robust shock-capturing. In Section 4, the details of the structured curvilinear overset grid-system used are provided. Sections 5 and 6 include the results and discussion for the two configurations studied, and some concluding remarks are made in Section 7.

## II. Wall modelled treatment in Large Eddy Simulations

While the majority of simulations presented in this paper are wall-modelled Large Eddy Simulations (WMLES), one of the cases (wing-only, 4.25° angle-of-attack) has been also recomputed using a Delayed Detached Eddy Simulation (DDES) on the RANS grid. As such, we will briefly review both methods in this section and provide details specific to our implementation and simulations. The schematic shown in Figure 3 illustrates the two wall-treatments.

### A. Wall-modeled Large Eddy Simulations

The work presented in this paper uses an equilibrium wall model (no-wall parallel grid connectivity) based on an analytic wall-function [35] to evaluate the wall-shear stress using the velocity at the exchange location. While the suction side of the wing experiences supersonic flow resulting in a shock, the adiabatic treatment of the wall and the relatively low supersonic Mach numbers (maximum Mach number never exceeds 1.45 in the irrotational regions of the flow) leads to boundary layer turbulence lacking any significant compressibility (friction Mach numbers, $u_\tau/c \ll 0.1$). Note that even at hypersonic Mach numbers, boundary layer turbulence lacks significant compressibility effects [36] since the intense aerodynamic heating results in very low density and high viscosity near walls, although the van-Driest transform is necessary due to density variations in the boundary layer at high Mach numbers[37]. The reader is referred to the recent work by Iyer & Malik (2019)[38] for a detailed discussion of modeling errors for adiabatic and non-adiabatic (cooled) walls in high-speed flows. Their *a-priori* analysis shows that for adiabatic conditions standard equilibrium wall-modeling (with wall-density based $y^+$ definition/scaling) results in less than 3-4% error for wall-model exchange locations as high as 30% of the boundary layer thickness for Mach 2 boundary layers. For further information regarding the applicability of an Equilibrium wall-model in highly non-equilibrium flows seen in shock-induced separation, the reader is referred to work by Bermejo-Moreno et al. (2014)[39] and recent reviews by Larsson et al. (2016) [40] and Bose & Park (2018) [41].

In the current formulation, the velocity fed into the wall-model is taken from the second off-wall point[40] and the returned wall-shear stress is used as a viscous flux boundary condition to the PDE solved at the first off-wall point after appropriate tensor rotations based on the transformation from local curvilinear coordinates to wall coordinates. Due to the use of a node-based solver with the first grid point located on the wall, some sensitivity to the choice of sided schemes used in the convective flux evaluation is observed (apart from sensitivities related to choice of the interior numerical scheme), although this discussion is beyond the scope of the work presented in this paper and needs to be described using simpler canonical problems.

### B. Delayed Detached Eddy Simulations

The Detached Eddy Simulation (DES) and Delayed Detached Eddy Simulation (DDES) turbulence model closures are well-tested hybrid RANS/LES models for highly separated flows. In the original DES model, the transition between RANS and LES models was based strictly on local mesh size relative to the wall-distance. For geometries with a wide range of geometric length scales, such as wings with finite-thickness trailing edges, the local mesh spacing may
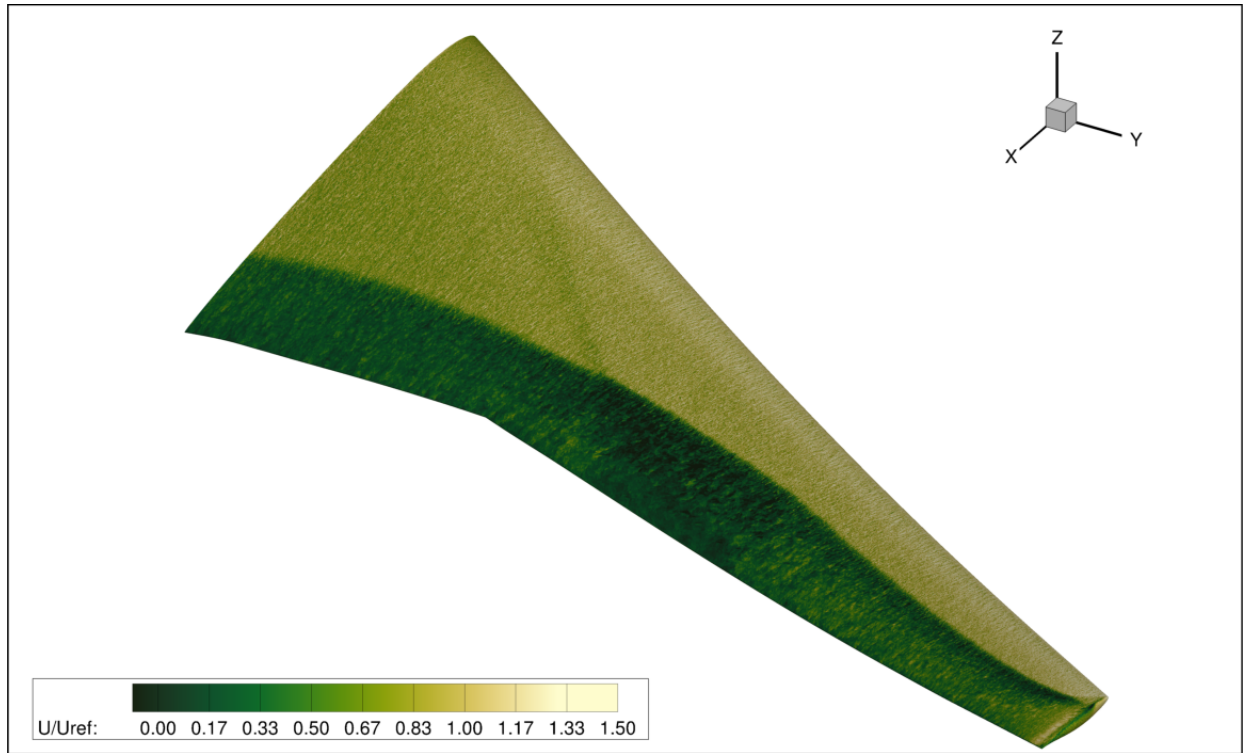
(a) Wing-only configuration (4.25° angle of attack)
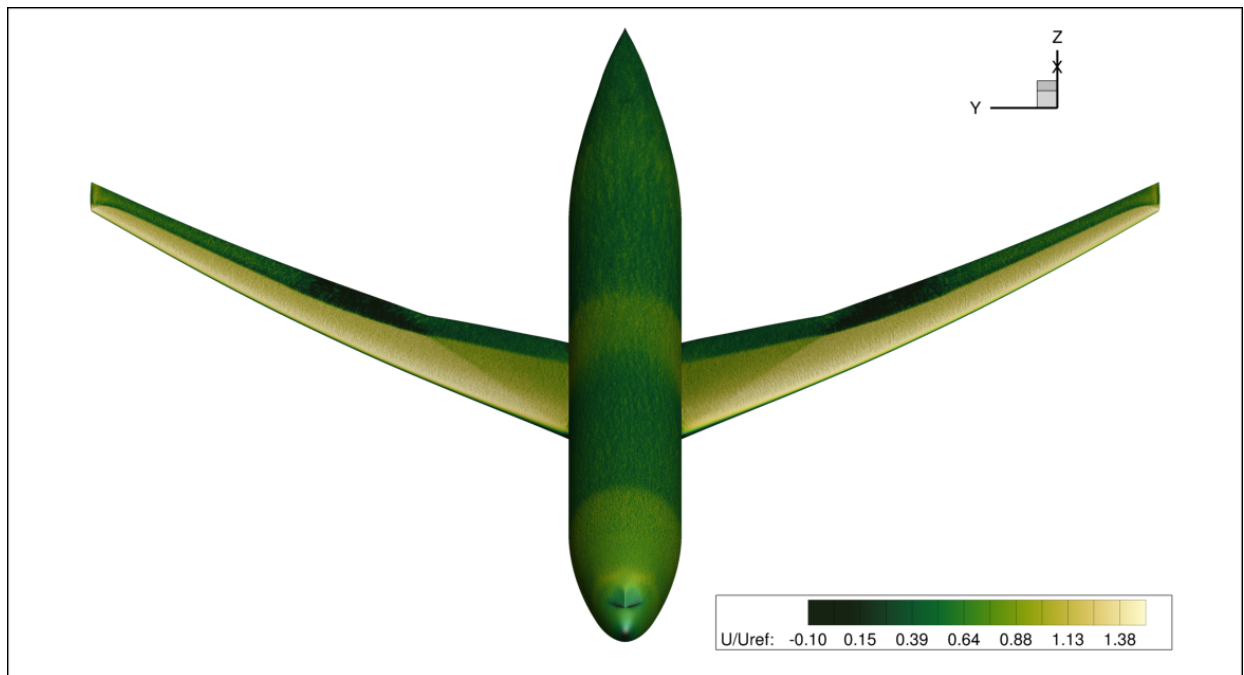


(b) Wing-body configuration (4.0° angle of attack)

**Fig. 2** **Streamwise velocity shown approximately $10^{-4}C_{ref}$ away from the surface for the two configurations studied using WMLES. A rigid/fixed wing geometry and mesh are used for the wing-only configuration at all angles of attack, whereas a different wing deformation is considered for the wing-body configuration for each angle of attack.**
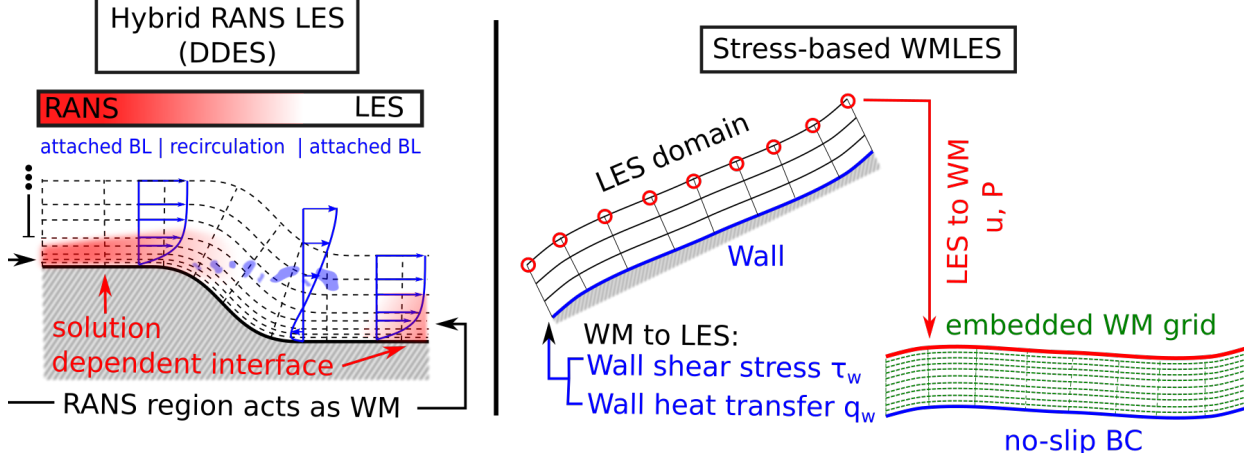
**Fig. 3  Schematic showing the differences between DDES and WMLES; a key difference between the two is that the exchange of information between LES and RANS domain in WMLES happens at separate locations, whereas this exchange in DDES happens via stencil-based dependence in adjacent nodes. The WMLES grid therefore circumvents the stiffness associated with the no-slip boundary condition in the LES domain, differentiating it with the grids used for RANS and DDES.**

become small enough to force transition from the RANS model to the LES model, but the mesh is typically not small enough to resolve the unsteady fluctuations causing the well-known modeled stress depletion [42]. This resulted in a modification denoted as DDES, which attempts to remain in RANS mode in the attached boundary layer [43]. The current implementation of the DDES model used for this work closely follows Zonal Detached Eddy Simulation (ZDES) Mode-II [44], where the primary differences from the original model are handling of the near-wall terms when in LES mode and the local length scale estimate. The DDES results reported herein (referred to as DDES2020) additionally use the *inhibition function* developed by Deck & Renard (2020) [45] to address the widely acknowledged [46–48] drawbacks associated with the default coefficients used in earlier versions of the indicator function.

## III. Numerical schemes

High-order accurate low dissipation finite-difference schemes have been shown to be an accurate and efficient strategy for turbulence resolving simulations using LAVA[28, 30, 33]. A thorough study comparing several high-order finite difference methods on Cartesian grids within the LAVA framework was reported previously[49]. Results from this study indicated that high-order Weighted Essentially Non-Oscillatory (WENO) schemes[50] performed well in both resolution (Points-Per-Wavelength PPW), shock capturing, and robustness under harsh flow conditions. A natural extension of finite-difference WENO schemes to curvilinear grids are the high-order Weighted Compact Nonlinear Schemes (WCNS)[51]. The WCNS method, applied to the convective fluxes, consists of a WENO or high-order interpolation (as opposed to reconstruction) of the left and right states to the half grid points, followed by an evaluation of the numerical flux at the half points by an approximate (or exact) Riemann solver or flux vector splitting scheme, and concluding with a high-order central finite-difference operator at the grid points which depends on the numerical fluxes at the half points in either an implicit (i.e. compact) or explicit form. When applying finite-difference methods to the curvilinear equations in strong conservation law form, standard WENO finite-difference methods will not satisfy the Geometric Conservation Law (GCL) making it necessary to combine the WENO interpolation with high-order central-difference operators. It has been shown that free-stream preservation (i.e. the GCL condition) is satisfied up to machine precision provided that identical central difference operators are used for discretizing the metric terms as well as the fluxes [52]. An additional advantage of WCNS over WENO is the ability to use approximate Riemann solvers. Standard finite-difference WENO methods require the use of flux vector splitting methods for numerical flux evaluation. In this work, the standard HLL numerical flux is used [53]. A consequence of using high-order central difference operators applied to numerical fluxes at the half grid points, which depend on high-order left and right state interpolations, is a much wider stencil required for the same order of accuracy compared to standard nodal finite-difference methods. To remove this pathology, high-order central difference operators using a combination of
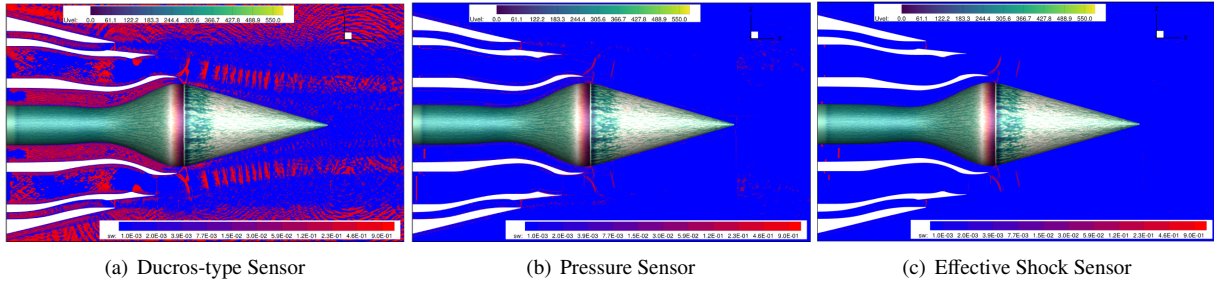
5

(a) Ducros-type Sensor          (b) Pressure Sensor          (c) Effective Shock Sensor

**Fig. 4  Shock sensors used to apply spatially localized upwinding in WMLES of a heated jet in the Top Mounted Propulsion Test (TMP17).**
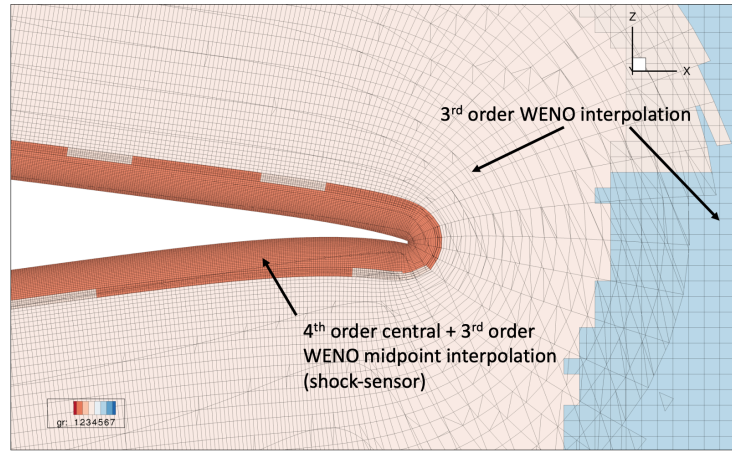


**Fig. 5  Numerical discretization used in different overset zones: the near-body regions use non-dissipative numerical discretization to resolve boundary layer turbulence, whereas the off-body and farfield zones use 3rd order WENO discretization.**

the numerical fluxes at the half grid points and the physical fluxes at the grid points have been developed [54, 55]. This approach, denoted Hybrid Weighted Compact Nonlinear Scheme (HWCNS), allows for up to third/fourth-order accuracy using a five-point stencil by combining blended third- and fourth-order interpolation with a fourth-order hybrid central difference operator. The blending of an upwind biased and pure central variable reconstruction [56], has been generalized by the authors to variable interpolation. The blending factor which ranges between 0 (purely central) to 1 (purely upwind biased) is determined locally using a shock sensor. This shock is obtained via a combination of a Ducros-type sensor that isolates acoustics and shocks from vortical turbulence, and a Pressure sensor that isolates turbulence and shocks from acoustics. The effective shock sensor is assumed to be the minimum of the two sensor values, thereby isolating shocks from both turbulence and linear acoustics. An illustration of the sensor usage along with the resulting localized upwind blending is shown in Figure 4 using a WMLES of a heated jet studied in the Top Mounted Propulsion Test (TMP17)[57]. A detailed description of the implementation in LAVA is included in the appendix of Housman et al. (2016)[58].

In the current approach, the convective fluxes (and the metric-terms used within) are evaluated using a shock-sensor based blending between 3rd order WENO interpolation and 4th order central interpolation in the near-wall regions of the domain (Figure 5). The divergence operator for the flux is a simple second order staggered difference operator. The regions of the domain containing irrotational flow are discretized using 3rd order WENO interpolation (without any use of a shock sensor) and the viscous fluxes (and their metric terms) are discretized with second-order accurate central differencing. The wall-modelled LES uses explicit time stepping based on TVD-RK3 [59] with a time step size determined by a CFL value of 1.25. The DDES result reported uses standard second-order accurate backward differencing (BDF2). For all the wall-modelled Large Eddy Simulations the constant coefficient Vreman SGS model[60] is used with a model constant of 0.06 (unless otherwise specified). Finally, a masking of the blended interpolation (of
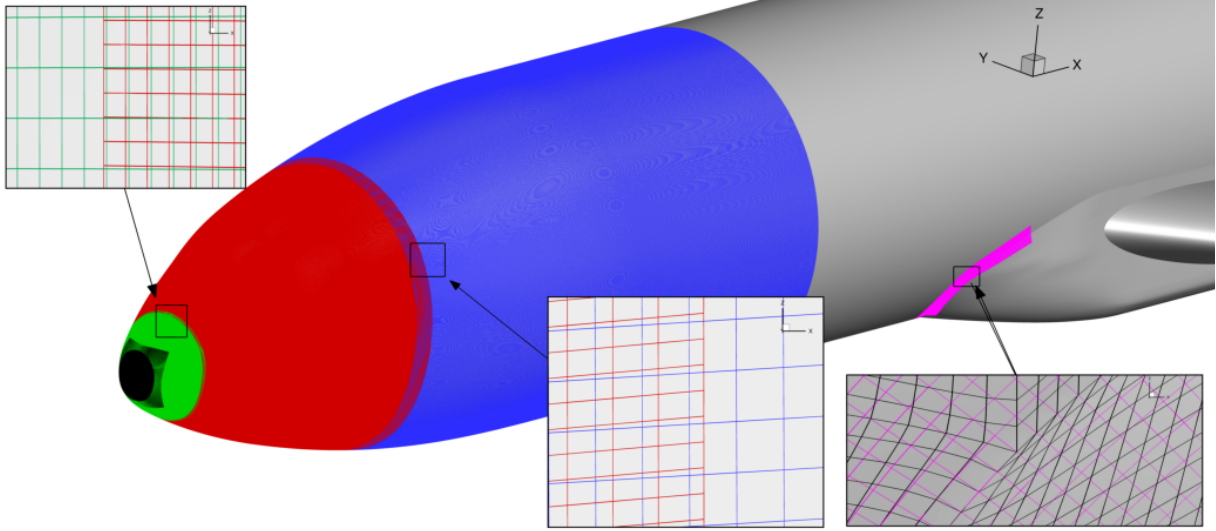
**Fig. 6  Overset meshes generated on the fuselage to accommodate the developing turbulent boundary layer and near the belly fairing to address the poor cell quality resulting in the underlying block-to-block topology.**

50% 3rd order upwind and 50% 4th order central) is performed near overset fringe points to enhance robustness and reduce numerical artifacts which may occur near overset boundaries using low dissipation schemes.

## IV. Structured overset grid systems

Structured curvilinear overset meshes are generated for WMLES for both the wing-only and the wing-body configurations. Care was taken to ensure that block-to-block grid topologies (as opposed to overset) could be adopted in the near-wall regions wherever possible, and the majority of the wing surface is meshed using entirely block-to-block topologies. This is pertinent since a major focus of the current study is to assess the ability of WMLES in predicting skin-friction drag and as described in Section 3, our numerical formulation relies on some localized unwinding at the overset fringe locations. However, note that at certain geometric interfaces such at the nose region and the belly fairing (see Figure 6), an overset grid was added to the underlying point-matched block-to-block surface grid in order to avoid poor mesh quality resulting from extraordinary corners in these regions. This is particularly relevant in the nose region where presence of such mesh-induced asymmetry in transitional part of the domain can persist downstream, contaminating the solution by adding a strong grid-dependency. Figures 7 and 8 show the volume mesh grown out of the surface mesh using two sets of multi-grid type coarsening levels. The growth distance of the innermost level (green in Figure 8) was ensured to be sufficient for accommodating the entire boundary layer; estimates for the boundary layer thickness were made using scaling laws for zero-pressure gradient boundary layers and were later verified using both RANS simulations and the final WMLES simulations. An attempt was made to use wall normal grid spacings and stretching ratios for resolving boundary layers with at least 15-20 grid points, although it is important to acknowledge the ambiguity in the definition of boundary layer thickness in the transition parts of the flow near the wing leading edge and the fuselage nose. At this point it is important to acknowledge that while our juncture flow numerical experiments [29] suggested the need for near-unity aspect ratio cells in the corner to capture corner-flow separation accurately, such high resolution has not been used in the present simulations since the focus is primarily on mid- and out-board regions of the wing where shock-induced separation occurs. Figure 10 shows the effective stream, span and wall-normal mesh spacings used along with the effective aspect ratios of the near-wall cells. While the inboard section contains aspect ratios as large as 7.5 near the root, care was taken to build a grid with less than 4 aspect ratio for the outboard spanwise station, $\eta > 0.5$. A summary of total number of grid points used in the overset grid system is provided in Table 1. Finally, note that at this time no attempt has been made for shock-aware grid refinement and the same grid is used to study all angles of attack. This is expected to result in some under-resolution with increasing angles-of-attack; future studies will attempt to address some of the observed drawbacks with systematic grid refinement, along with strategies to address under-resolved LES via enrichment [61, 62].
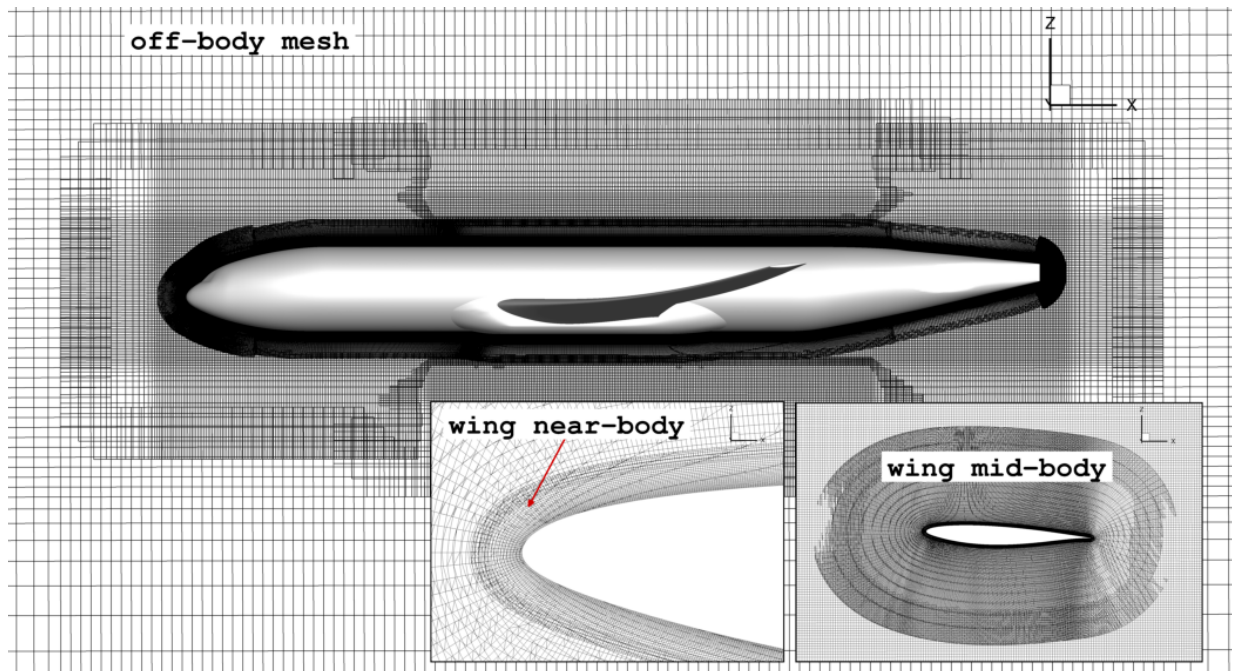
**Fig. 7   Off-body coarsening used in the outer potential flow in order to reduce the total number of grid points while maintaining sufficient resolution to capture the transonic shock that occurs on the wings.**
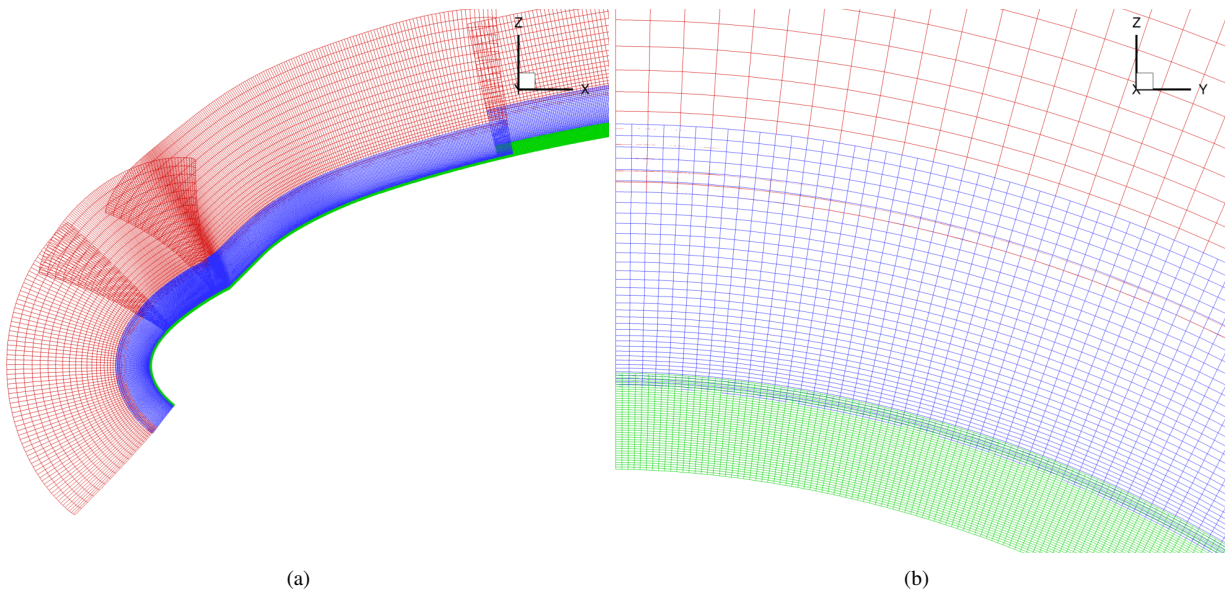


(a)                                                                                              (b)

**Fig. 8   Surface mesh is grown away from the body with three layers of multi-grid type (factor of 2) coarsening. This allows for generation of sufficient overlap with the substantially coarser off-body Cartesian mesh without compromising resolution needed to resolve the boundary layer turbulence.**
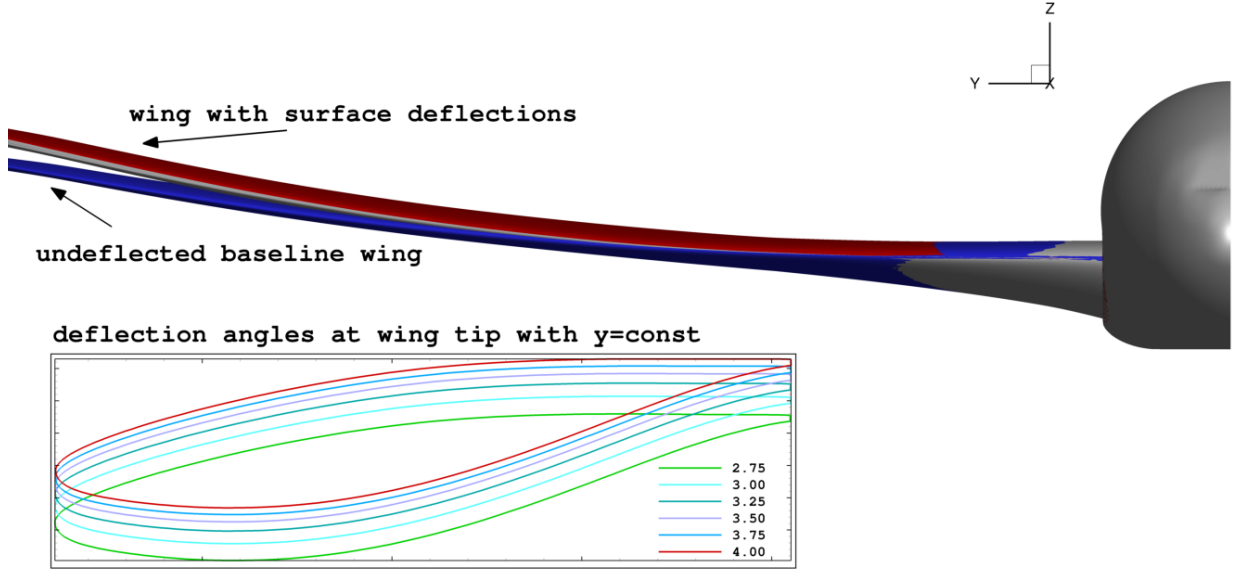
**Fig. 9  Wing surface and mesh deflections used for the 6 angles of attack studied using WMLES.**

| Mesh Type | Fuselage | Juncture | Wing | Off-body | Total points |
|---|---|---|---|---|---|
| Wing-body (full-span) | 244 | 14 | 402 | 22 | 682 |
| Wing-only | - | - | 166 | 40 | 206 |

**Table 1  Summary of grid points used in the two overset grid systems. Reported numbers are in millions of grid points.**

All the WMLES were run using an explicit time step determined with a CFL number of 1.25. For all angles of attack studied, this time step size was approximately, $8 \times 10^{-5} c_{ref}/U_{ref}$, with each chord-based convective time unit (CTU) requiring about 12,000 RK3 time steps. The computational cost of 1 CTU simulated in the 682 million point wing-body grid system is approximately 3000 core hours (Intel Skylake) which is equivalent to approximately 120 NASA Standard Billing Units (SBUs) per CTU. The majority of the simulations were run for at least 50-60 CTUs with the higher angles of attack requiring significantly larger times (more than 100CTUs) because of low frequency oscillations in the shock position.

The RANS simulations for the wing-only configuration used coarse (4 million grid point) and medium (29 million grid point) sized grid systems while publicly available (see supplementary material from Lyu et al., 2014 [6]) grid systems were used for steady state simulations. The single DDES reported in the paper used the coarse RANS grid (4 million grid points) with a fixed time step size of $3 \times 10^{-4} c_{ref}/U_{ref}$. The computational cost of each CTU simulated is approximately 516 core hours (Intel Skylake) which is equivalent to approximately 21 SBUs per simulated CTU.

The wing-body meshes incorporated deflected shapes that were measured during wind-tunnel experiments. As shown in Figure 9, there is a small amount of deformation between the un-deflected or "jig shape" and the "flying shape" at each angle of attack. The wing deformation induces a small amount of additional wing-twist which results in lower lift values for a given angle of attack as compared to the baseline configuration. Note that while the baseline wing is designed to match the shape of a real deformed wing, further deflections of the wind-tunnel model wing are inevitable and it is these smaller corrections that we are accounting for with the individual meshes for each angle of attack.

Both the wing-only and wing-body configurations use farfield BCs located at least 100 reference chord units away from the body. The farfield BCs are based on Riemann invariance conditions. The wing-only configuration uses a symmetry plane BC at the wing root. Note that while this type of boundary condition in LES is not entirely consistent with its usage in RANS, the effect of the effective no-penetration condition is only felt up to spanwise distances of the order of the boundary layer thickness. Hence, no additional treatment was deemed necessary for comparisons between
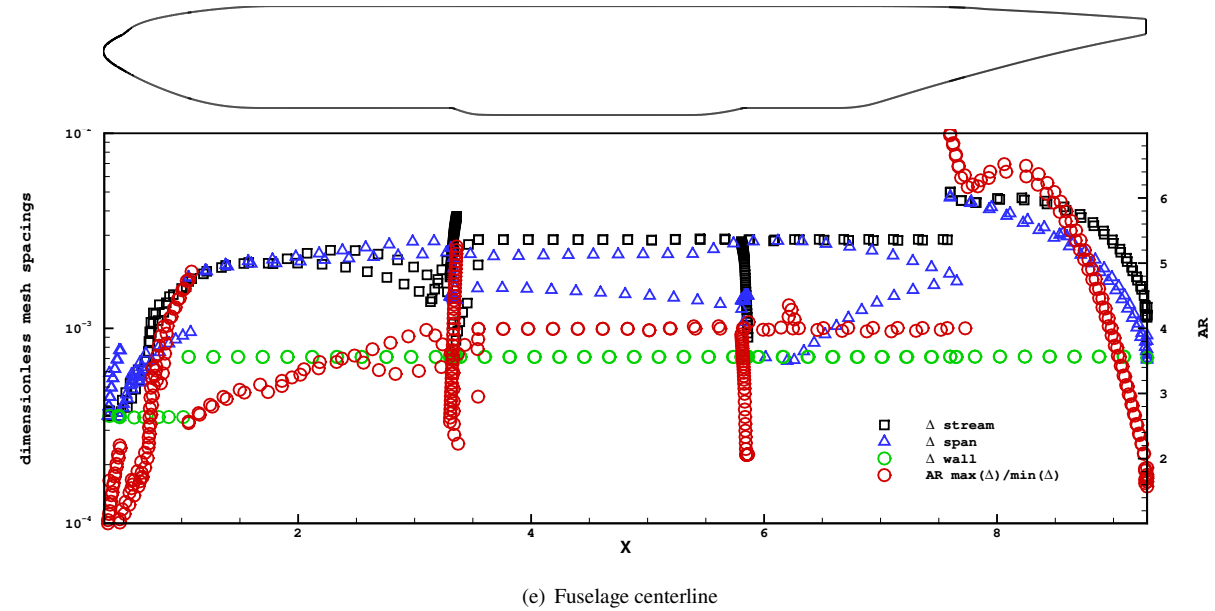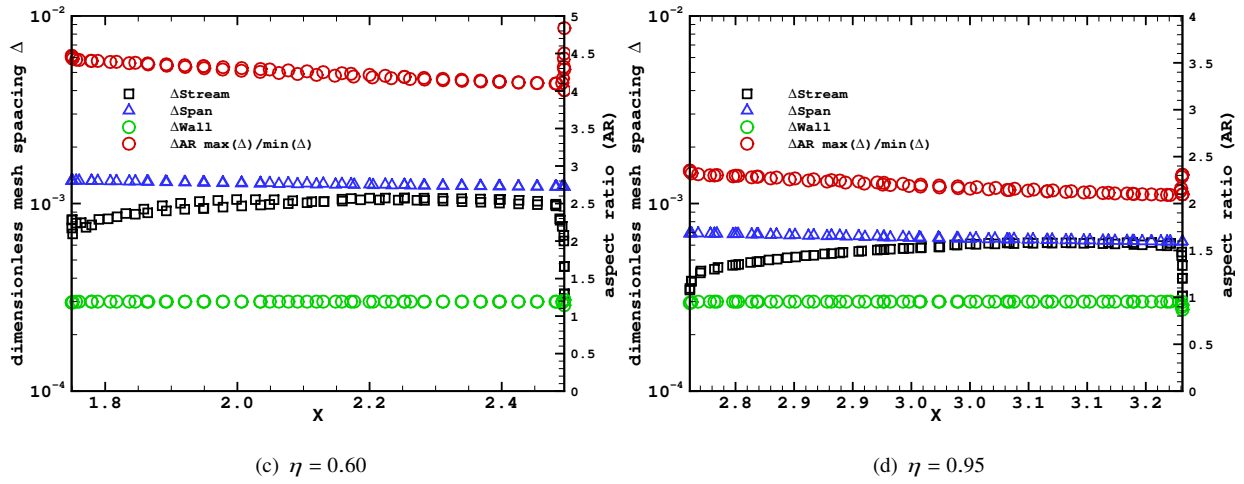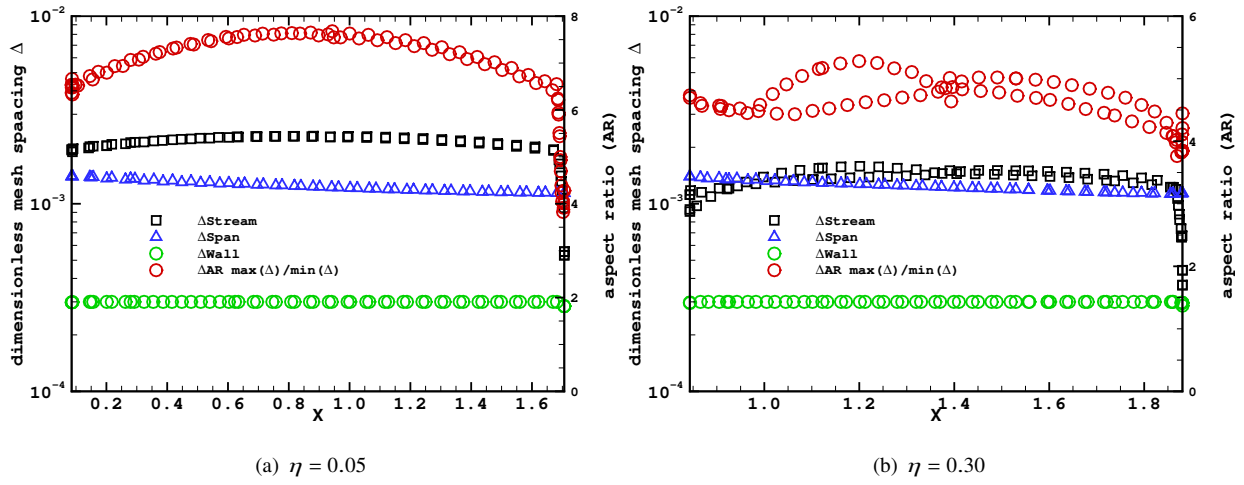
(a) $\eta = 0.05$

(b) $\eta = 0.30$

(c) $\eta = 0.60$

(d) $\eta = 0.95$

(e) Fuselage centerline

**Fig. 10    Mesh spacings in the near-wall zones of the overset grid system used for the wing-body configuration.**

RANS and WMLES.

## V. Results for the wing-only configuration

We begin the discussion of the results by first considering the wing-only configuration where we compare the WMLES results with those obtained using two popular RANS models: a) SA-RC-QCR2000[63] and b) $k - \omega$ SST[64]. While this configuration does not experience any corner flow, all RANS simulations with the SA model still made use of the quadratic correction (QCR). Note that all the WMLES shown here use a time averaging interval of more than 50 crank-chord based flow units ($C_{Ref}/U_{ref}$). The reader should note that Figures 11 through 16 pertain the the angle of attack, $alpha = 2.5°$ case. Figure 11 shows the comparison of the lift coefficient, the total drag coefficient and the viscous drag contribution for two RANS grids and the WMLES at three different values of the Vreman model constant. Sensitivity to SGS model coefficient is less than 2% for all three coefficients, and appears to be of the same order of magnitude as the difference between the two RANS models in their respective asymptotic limits. Furthermore, it is interesting to note that the skin-friction drag ($C_{DV}$) appears to be quite accurately predicted by the LES with all three coefficient values resulting in a prediction that is within 1-2 drag counts of the asymptotic values of the RANS solutions. Further insight into the sensitivity of the model constant to the predicted aerodynamic loads can be seen by comparing the surface pressure coefficients and skin friction coefficients, as is done in Figures 12 and 13 respectively. It is very apparent that while the pressure shows little sensitivity to the model constant, the transitioning boundary layer near the leading edge does show quite a sensitivity in terms of the skin friction. Note that since all the WMLES use numerical transition with no explicit representation of obstructive tripping (that is typically used at such low Reynolds numbers in experiments), such sensitivity is entirely expected especially in the severely under-resolved transitional boundary layers. This can be further observed in terms of the surface skin friction contour plots comparing the WMLES (at a model constant of 0.06) with the two RANS simulations in Figure 14. While these plots confirm the overall agreement in skin friction drag shown in Figure 11, they do highlight an important attribute of both the RANS and the WMLES in the outboard portions of the wing. While it is clear that the WMLES over-predicts the skin friction coefficient in transitional boundary layers, this over-prediction is particularly relevant in the outboard sections of the wing where the shock moves closer to the leading edge. This sensitivity is also observed between the two different RANS models which have non-universal behavior in very low-Reynolds number boundary layers. To further characterize this low-Reynolds number effect in the outboard regions of the wing, we characterize the Reynolds number associated with the streamwise location of the shock as a function of spanwise location in Figure 15. Based on this plot, we argue that for spanwise stations where $Re_x^{shock} > 2 \times 10^6$, excellent agreement is obtained between the two RANS models and WMLES. This can be confirmed using the pressure coefficient comparisons shown in Figure 16 where quantitative disagreements are only seen at the spanwise location, $\eta = 0.9$. Note that the over-peak in negative cp seen in the outboard section of the wing in WMLES is associated with numerical transition, resulting in small underprediction of lift and a slight modification to the pressure drag by about 1.5%; this sensitivity was assessed by stencil-based numerical modifications in the transitioning regions of flow. While this overshoot can be remedied by careful treatment of numerical transition using obstructive tripping, it was not deemed important in the present work since it is largely an artifact of the low-Reynolds number simulated.

Given the promising agreement between RANS and WMLES at the $\alpha = 2.5°$ angle of attack, we now consider the comparison between the methods at various angles of attack ranging from 1° to 5.25°. Figure 17 shows the lift curve and the drag polar comparing WMLES and RANS. It is evident that in the linear regime ($C_L < 0.64$) the two methodologies agree. However, for $C_L > 0.64$ RANS shows a sharp break away from the linear regime as it predicts onset of shock induced flow separation. This onset is predicted at an angle of attack of approximately 0.5° higher in WMLES with a corresponding $C_L = 0.69$. In order to understand this difference, we conducted a DDES at an angle of attack, $\alpha = 4.25$. Note that this DDES uses the new shielding function developed in Deck & Renard (2020)[45] and hence we refer to it as DDES2020. This hybrid RANS/LES uses the coarse RANS mesh and a fixed explicit time step of $\Delta t = 3 \times 10^{-4}$. It is promising to see that the mid- and out-board unsteadiness in the shock, triggered by the use of DDES results in a downstream shift in the time-averaged shock location. This can be seen in the pressure coefficient comparisons shown in Figure 18. Note that in this result, the DDES flow fields have been averaged over a time interval of at least 30 crank chord based flow units ($C_{Ref}/U_{ref}$). Furthermore, note that the drag predicted by the DDES and WMLES largely agree at $\alpha = 4.25$, which is likely a consequence of similar induced drags seen in the two simulations. Finally, we consider the sensitivity of the skin-friction drag prediction to the angle of attack in Figure 19. While all simulations predict a reduction in overall skin-friction drag with increasing angle of attack (due to upstream movement of the shock), the WMLES is notably about 1-2 drag counts higher than the fine mesh RANS simulations. To understand the
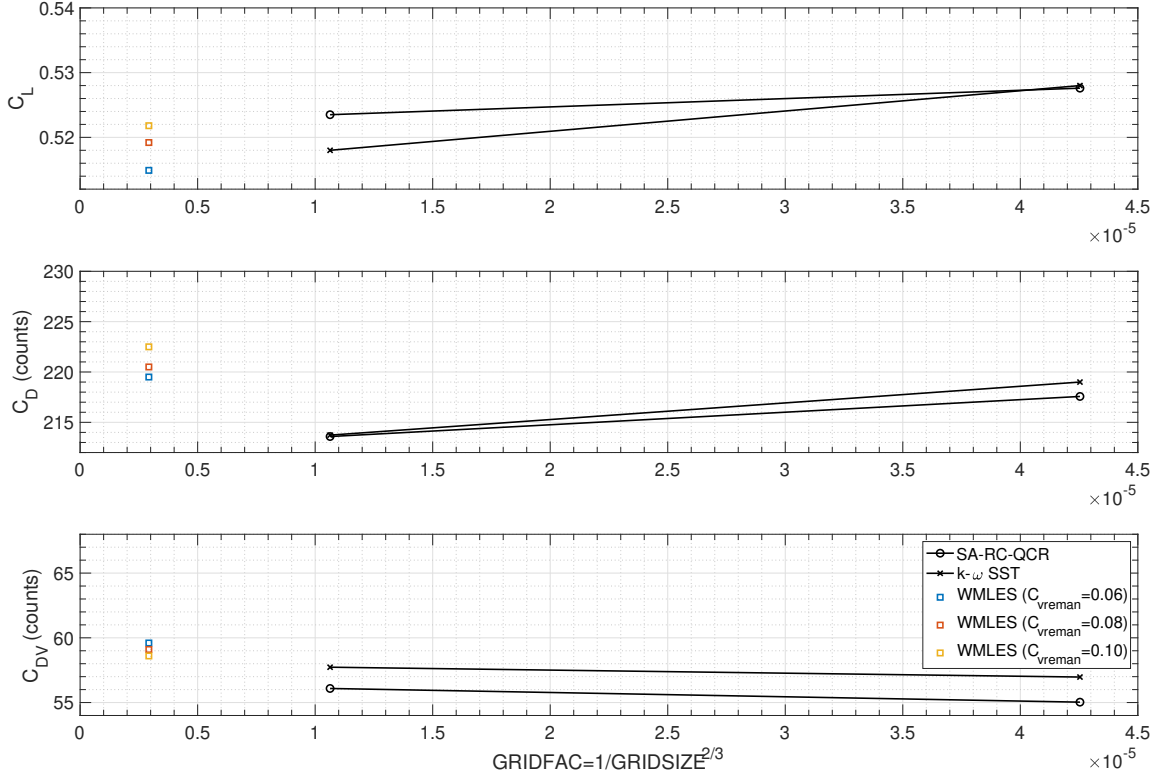
**Fig. 11 Comparison of non-dimensional lift and drag loads for the wing-only configuration at an angle of attack, $\alpha = 2.5°$ for varying SGS model constant and grid spacings.**

asymptotic trends in this over-prediction, two additional WMLES meshes with larger and smaller wall-normal spacings (but identical surface spacings) were created. Some small changes to the overall numerical transition mechanism occur with the changes in near-wall spacing which subsequently change the skin-friction drag by up to 1 count. While a more rigorous assessment is needed using systematic grid refinement in both wall-normal and wall-parallel directions, it is nonetheless promising to observe that both WMLES and RANS appear to have consistent trends approaching very similar skin-friction drag values in their asymptotic limits. The DDES at $\alpha = 4.25°$ sees an increase in the skin-friction drag compared to the steady state simulation on the identical grid; this increase is caused by a slight downstream shift in the time averaged shock location in the outboard sections of the wing.

## VI. Results for the wing-body configuration

We begin the discussion of the full wing-body configuration by first considering the pressure distribution at several spanwise stations on the wing. As was done in Tinoco (2020)[7] using RANS data, in order to assess the accuracy of our WMLES predictions, we consider comparisons with experimental data obtained from three facilities: a) The National Transonic Facility (NTF), b) the Ames 11-foot Transonic Wind Tunnel Facility, and c) the European Transonic Wind Tunnel Facility (ETW). Note that while the experiments used tripping on wings[65] at approximately 10% chord, all the WMLES results reported herein relied on numerical transition near the leading edge. The reader is referred a series of papers by Rivers et al. (2011-2015) [65–68] for further information, including investigations of the aeroelastic effect and influence of the support system. In this work, we use the wing twist and bending provided at various angles of attack as part of DPW-6 to account for *static aeroelasticity* and perform all simulations as idealized *free-air* simulations.

Figure 20 shows comparison of the pressure coefficients obtained at an angle of attack, $\alpha = 2.75°$ compared with the Ames experiment at a similar angle of attack. Note that while the shock positions seem to be captured quite accurately, there is some evidence of the so-called *aft-loading* near the trailing edge in the outboard sections of the wing. This peculiar over-prediction appears to be entirely consistent with all other RANS submissions as part of DPW-6 and results
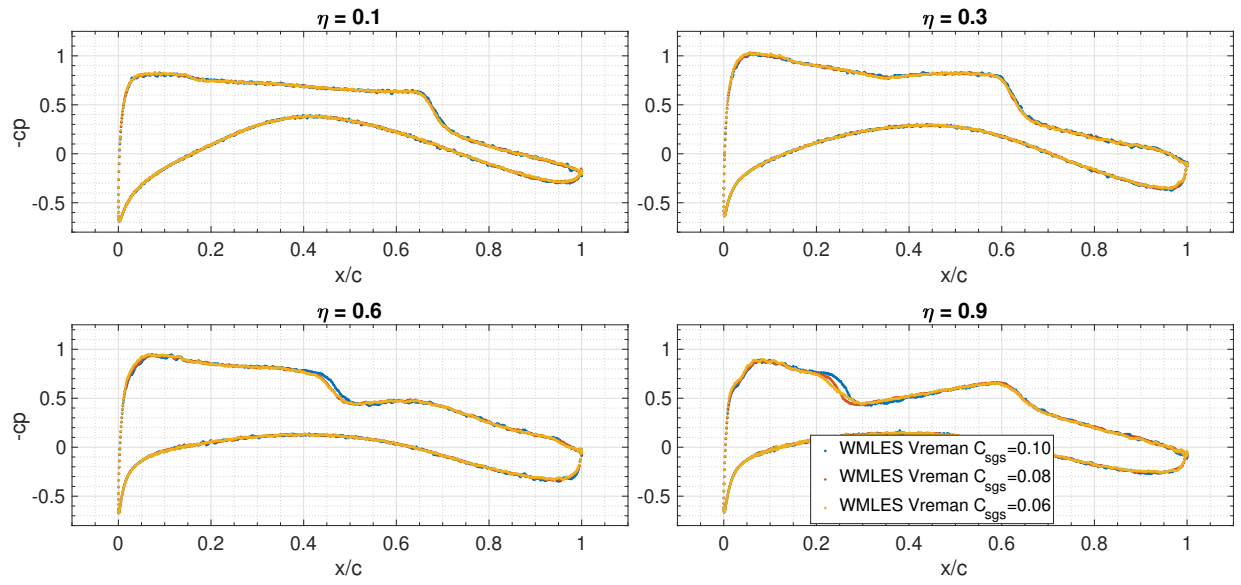
**Fig. 12    Sensitivity of Pressure coefficient to subgrid scale model constant at four spanwise locations.**
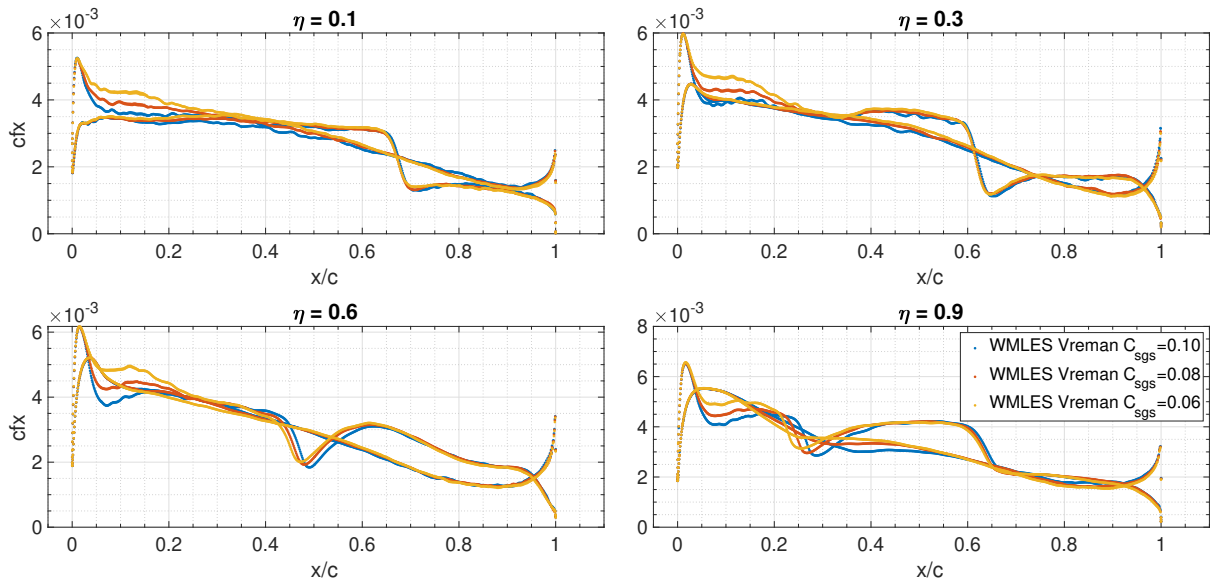


**Fig. 13    Sensitivity of Pressure coefficient to subgrid scale model constant at four spanwise locations.**
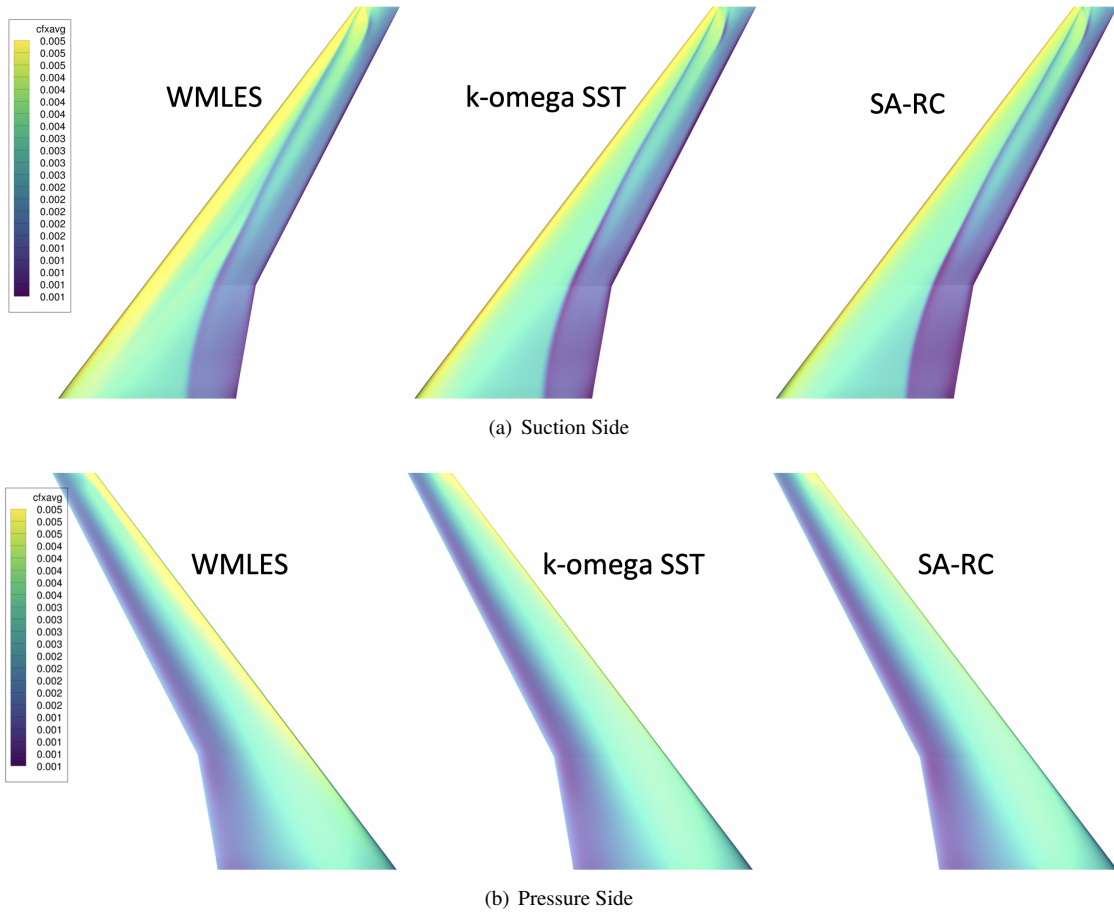
(a) Suction Side



(b) Pressure Side

**Fig. 14    Skin friction coefficient (streamwise) on the wing surface at an incident angle-of-attack, $\alpha = 2.5°$.**



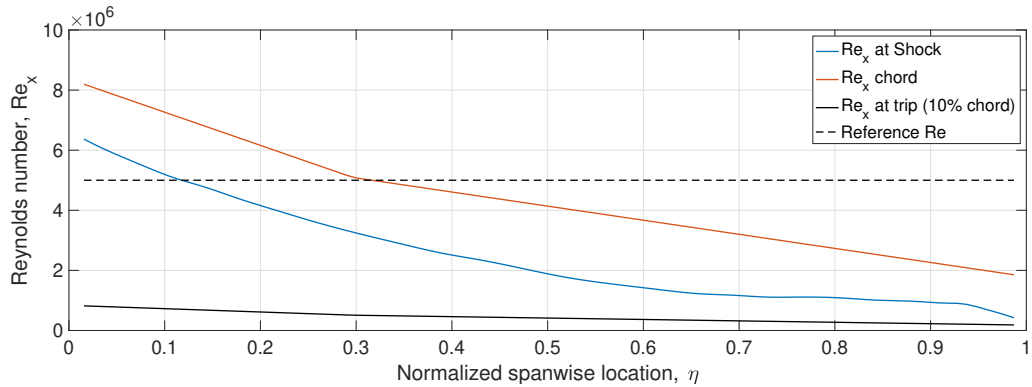**Fig. 15    Reynolds numbers based on the streamwise location of various features including the shock location as a function of spanwise location. This plot was generated using the suction side skin-friction coefficients (streamwise) obtained using SA-RC-QCR RANS closure at an incidence angle of attack, $\alpha = 2.5°$.**
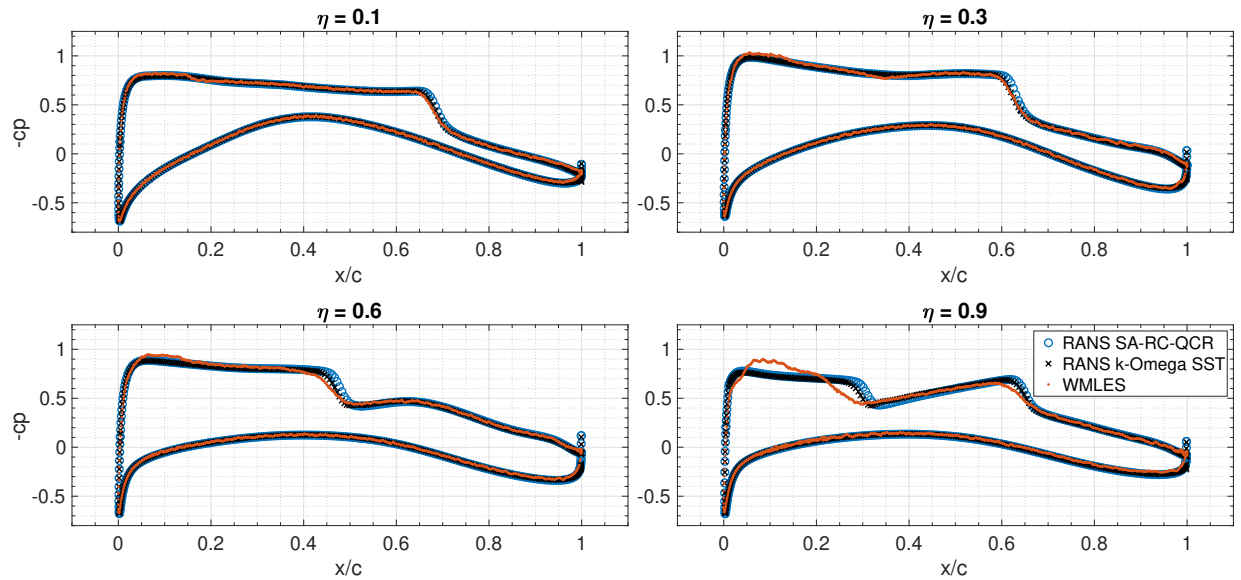
**Fig. 16   Comparison of pressure coefficient at various spanwise locations between RANS and WMLES (model constant is 0.06) at an incidence angle of attack, $\alpha = 2.5°$.**
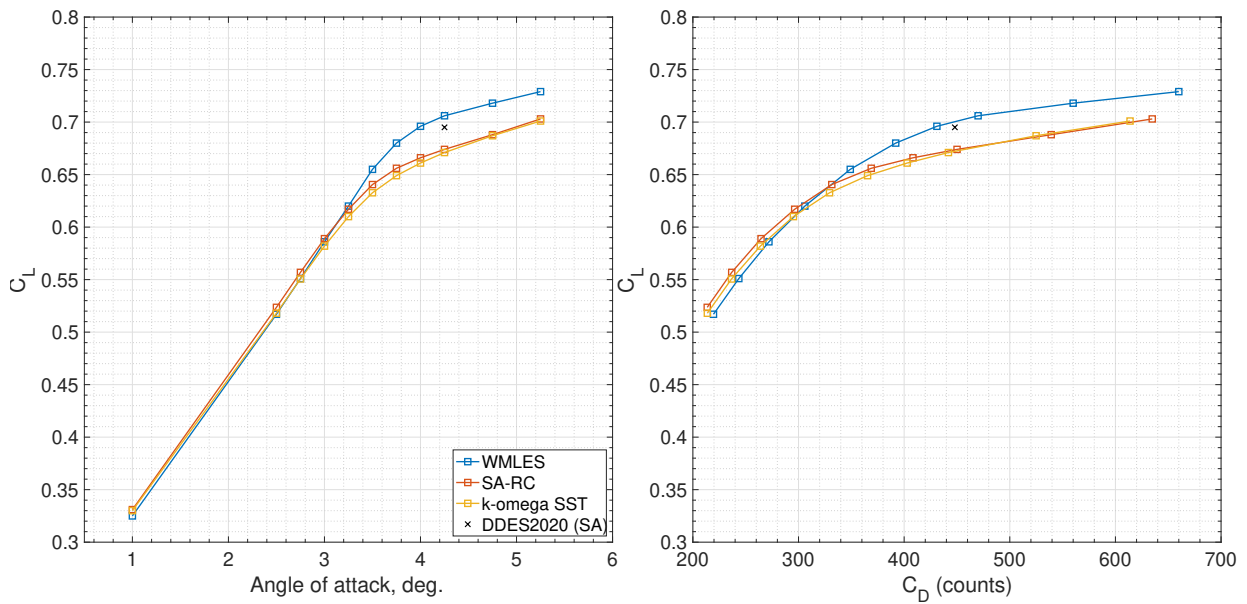


**Fig. 17    Lift and Drag coefficients as a function of angle of attack for the wing-only configuration.**
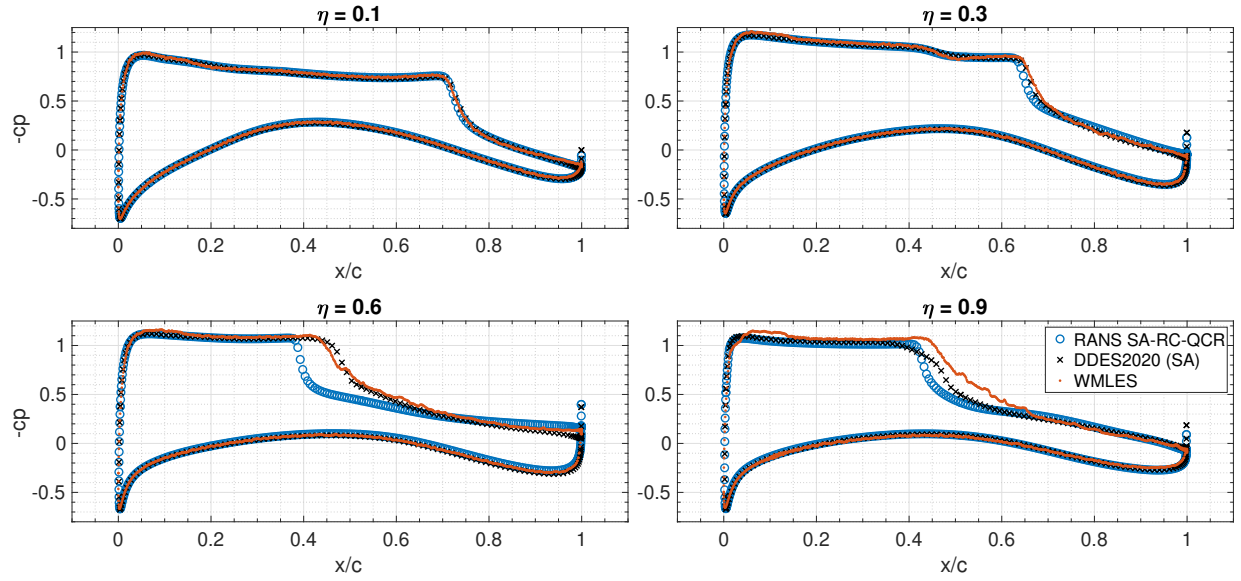
**Fig. 18  Pressure coefficient comparisons between WMLES, DDES and RANS using SA-RC-QCR at an angle of attack,** $\alpha = 4.25°$.
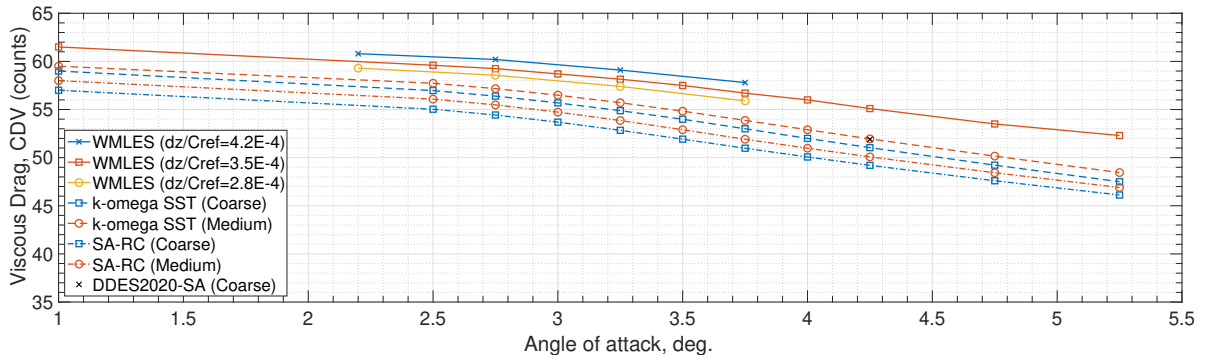


**Fig. 19  Skin friction drag comparisons between the three simulation methodologies as a function of angle of attack for the wing-only configuration.**

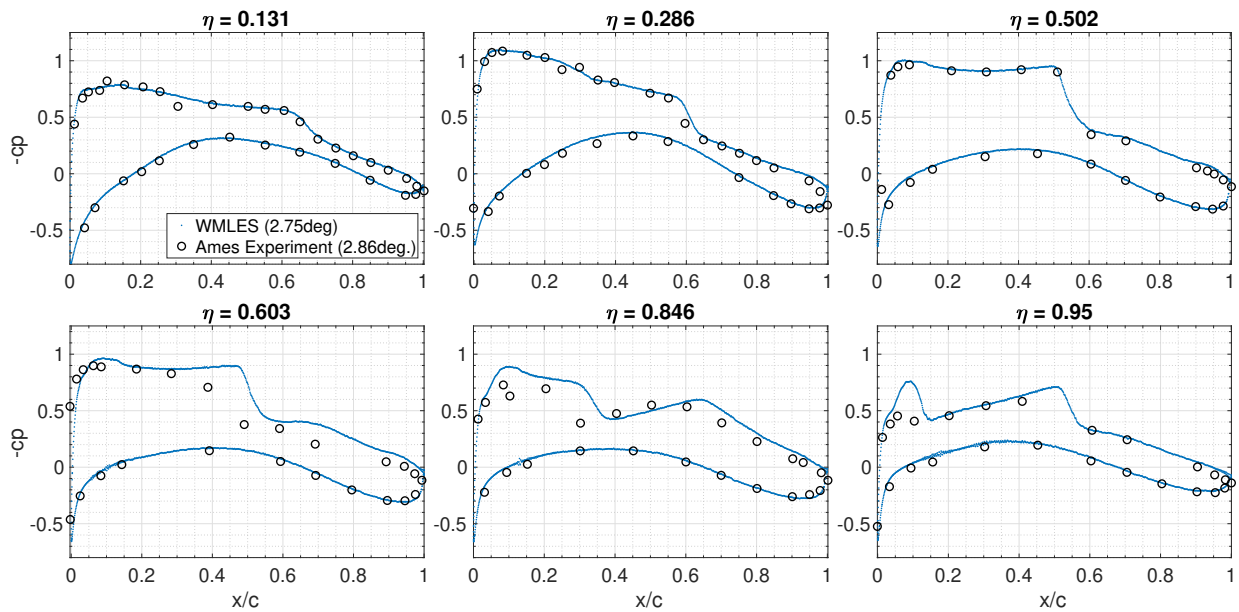**Fig. 20** **Pressure coefficient comparisons between WMLES and experiments at angle of attack of** $2.75°$ **corresponding to a** $C_L \approx 0.5$**.**
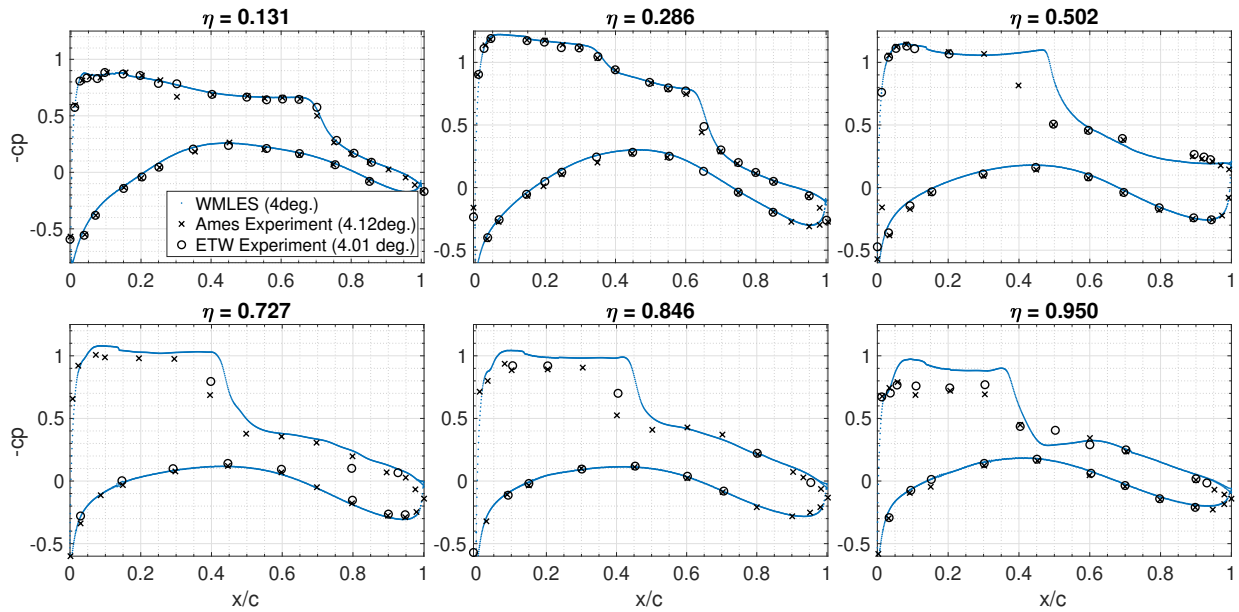


**Fig. 21** **Pressure coefficient comparisons between WMLES and experiments at angle of attack of** $4°$
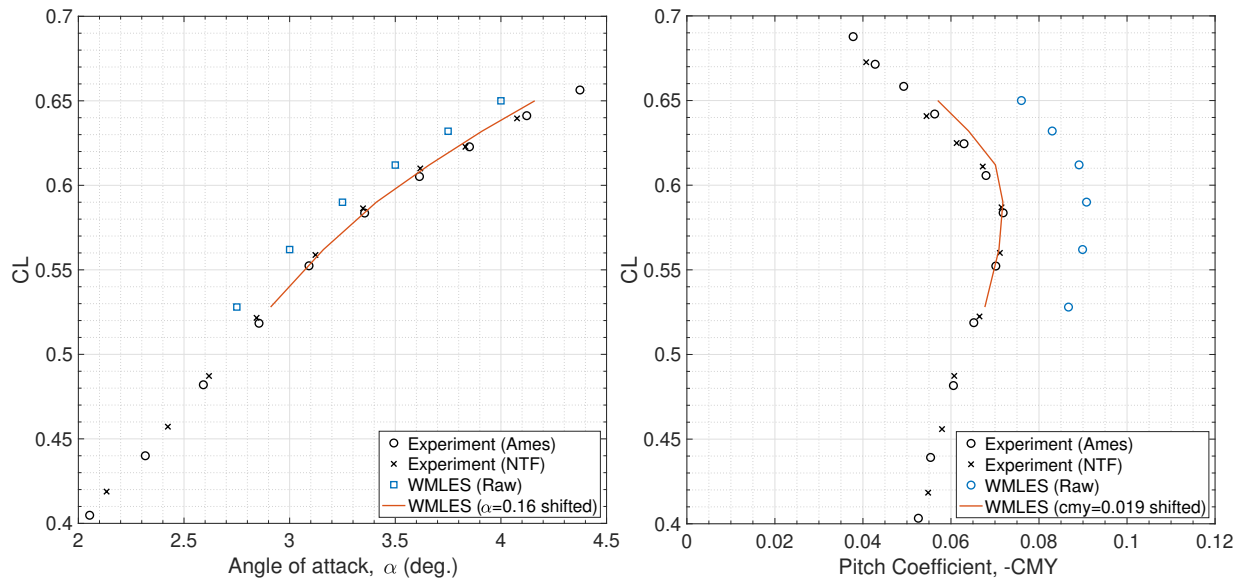
**Fig. 22  Lift Coefficient and Pitching moment of varying angles of attack. Note that the shifted data follows the CL-matching at $CL = 0.53, \alpha = 2.91°$ as introduced by Tinoco (2020)[7]. This corresponds to a angle of attack shift of $0.16°$. The pitching moment $c_m$ was shifted by $cm = 0.019$ also based on the procedure used in Tinoco (2020)[7].**
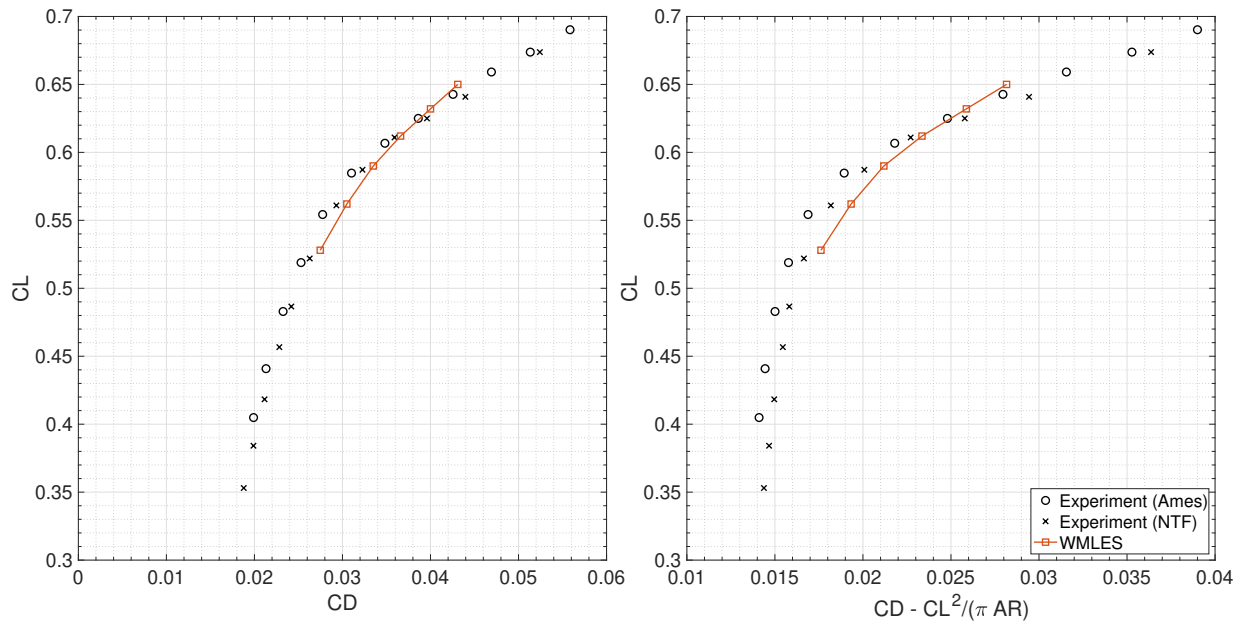


**Fig. 23  Drag polars obtained using WMLES for the wing-body configuration.**

in slightly excess lift coefficient and excessive pitching moments. At this time it is unclear if further resolution will mitigate this, although we note that sensitivity to tripping of the boundary layer is expected in the outboard sections of the wing due to the aforementioned low Reynolds number at shock-incidence. We further note that a second source of uncertainty in such comparisons between WMLES and experimental data is the potential for mischaracterization of aeroelasticity using static deflections mostly in the outboard sections of the wing. Next, we consider the pressure coefficient comparisons at post-separation angle-of-attack of 4° in Figure 21. Here it becomes evident that agreement in the inboard sections of the wing is excellent but the location of the shock in the outboard regions is not very accurate, with the WMLES predicting a shock located further downstream compared to observations in both Ames and ETW experiments. Furthermore, note the overprediction in negative cp upstream of the shock at the two outboard sections; this is again a consequence of numerical tripping along with the low-Reynolds numbers seen. At this time, it is clear that additional span and streamwise resolution might be needed in mid- and out-board regions of the wing experiencing shock-induced separation and unsteady buffeting. Nonetheless, we note the overall promising agreement observed using the relatively coarse resolutions, and the errors seen in WMLES at the 4° are very similar to some of the best RANS submissions at DPW-6 (identified as the *selected* cases in Tinoco (2020)[7].

Finally, the lift coefficient and the pitching moment as a function of the angle of attack are reported in Figure 22. It is interesting to observe that while the raw WMLES data suffers from the same overpredictions seen in all RANS results, an angle of attack shift of approximately 0.16° results in lift coefficients that match the experiment quite accurately. Both the lift-curve slope and the the pitch-break at approximately 3.5° angle of attack seem to be accurately predicted. Similarly promising agreement in the drag polar is seen in Figure 23. In the second subfigure, we consider the difference between the total drag and the idealized induced drag in an attempt to study the agreement between the expected wave drag. While the agreement is reasonable, we acknowledge that the drastic increase seen in the experimental data with increasing angle-of-attack is somewhat subdued in WMLES observations. Further grid-refinement is needed in WMLES to investigate this aspect further.


## VII. Conclusions

The primary focus of this work is to assess the ability of Equilibrium Wall-Modelled Large Eddy Simulations to predict aerodynamic forces and moments on a representative tube-and-body aircraft geometry at transonic conditions leading up to and including the onset of shock-induced flow separation and buffet. A secondary objective was to validate the WMLES framework with LAVA for high-speed transonic flows seen in many applications in external aerodynamics. Both goals were addressed via systematic study of two geometry configurations: a) Wing-only configuration that stays rigid with increasing aerodynamic loading, and b) the Wing-body CRM geometry with static aeroelasticity which served as a test case in the 6th AIAA Drag Prediction Workshop (DPW).

The wing-only configuration is used to demonstrate the sensitivity of the skin-friction coefficient to the SGS model constant; while some sensitivity is seen in transitional regions of the flow this sensitivity is largely consequential only in outboard regions of the wing where the Reynolds number at shock incidence ($Re_x$) is about $10^6$. It is shown that despite these uncertainties, the effective viscous drags predicted by WMLES is in excellent agreement with the two RANS results. Some basic grid refinement in the wall-normal direction is shown to reduce the over-prediction of skin-friction near the leading edge leading to a decrease in the skin-friction drag of about 1 drag count; the asymptotic skin friction drag values appear to be in excellent agreement with the WMLES predictions. While both RANS and WMLES show good agreement in lift and drag values in the linear regime of the lift curve, the break associated with onset of shock-induced separation occurs at roughly 0.4° lower in RANS compared to WMLES. This is further investigated by using a Delayed Detached Eddy Simulation (DDES) which appears to be in better agreement with the WMLES results compared to the RANS predictions.

The second part of the study considers the full wing-body configuration with comparisons made between WMLES and experimental measurements obtained from three separate facilities. It is interesting to note that the phenomenon of *aft-loading* seen in every single RANS result from DPW-6, is also present in WMLES. Based on the $\alpha$-shifting procedure specified in Tinoco (2020)[7], the WMLES is shown to have promising agreement with experimental data, including the prediction of the pitch-break that occurs at the onset of shock-induced separation. Some over-prediction of lift is observed post shock-induced separation associated with outboard time-averaged shock locations occurring slightly downstream compared to the experimental observations. The drastic increase in wave-drag seen in experimental measurements is somewhat subdued in the WMLES predictions. Further work is needed using simulations with higher span and stream grid resolutions in the mid and out-board sections of the wing in order to better capture the increased shock-strength that occurs at higher angles of attack. These higher resolution simulations will also enable the

characterization of the unsteadiness in loading, along with tonal and broadband character of pressure fluctuations near the trailing edge associated with the self-sustained low-frequency shock oscillations that occur during transonic buffet.

## Acknowledgments

## References

[1] Kenway, G. K., Kennedy, G. J., and Martins, J. R., "Scalable parallel approach for high-fidelity steady-state aeroelastic analysis and adjoint derivative computations," *AIAA journal*, Vol. 52, No. 5, 2014, pp. 935–951.

[2] Sobieszczanski-Sobieski, J., and Haftka, R. T., "Multidisciplinary aerospace design optimization: survey of recent developments," *Structural optimization*, Vol. 14, No. 1, 1997, pp. 1–23.

[3] Jameson, A., "Re-engineering the design process through computation," *Journal of Aircraft*, Vol. 36, No. 1, 1999, pp. 36–50.

[4] Martins, J. R., and Lambe, A. B., "Multidisciplinary design optimization: a survey of architectures," *AIAA journal*, Vol. 51, No. 9, 2013, pp. 2049–2075.

[5] Kenway, G. K., and Martins, J. R., "Multipoint high-fidelity aerostructural optimization of a transport aircraft configuration," *Journal of Aircraft*, Vol. 51, No. 1, 2014, pp. 144–160.

[6] Lyu, Z., Kenway, G. K., and Martins, J. R., "Aerodynamic shape optimization investigations of the common research model wing benchmark," *AIAA journal*, Vol. 53, No. 4, 2015, pp. 968–985.

[7] Tinoco, E. N., "Analysis of the Transonic NASA Common Research Model at High Angle of Attack," *AIAA Aviation 2020 Forum*, 2020, p. 2745.

[8] Slotnick, J., Khodadoust, A., Alonso, J., Darmofal, D., Gropp, W., Lurie, E., and Mavriplis, D., "CFD vision 2030 study: a path to revolutionary computational aerosciences," 2013.

[9] Chaouat, B., "The state of the art of hybrid RANS/LES modeling for the simulation of turbulent flows," *Flow, turbulence and combustion*, Vol. 99, No. 2, 2017, pp. 279–327.

[10] Rumsey, C. L., Slotnick, J. P., and Sclafani, A. J., "Overview and Summary of the Third AIAA High Lift Prediction Workshop," *Journal of Aircraft*, Vol. 56, No. 2, 2019, pp. 621–644.

[11] Rumsey, C. L., "The NASA juncture flow test as a model for effective CFD/experimental collaboration," *2018 Applied Aerodynamics Conference*, 2018, p. 3319.

[12] Ganapathisubramani, B., Clemens, N., and Dolling, D., "Large-scale motions in a supersonic turbulent boundary layer," *Journal of fluid Mechanics*, Vol. 556, 2006, p. 271.

[13] Ganapathisubramani, B., Clemens, N., and Dolling, D., "Effects of upstream boundary layer on the unsteadiness of shock-induced separation," *Journal of fluid Mechanics*, Vol. 585, 2007, p. 369.

[14] McDevitt, J. B., Levy Jr, L. L., and Deiwert, G. S., "Transonic flow about a thick circular-arc airfoil," *AIAA Journal*, Vol. 14, No. 5, 1976, pp. 606–613.

[15] Lee, B. H., and Ohman, L., "Unsteady pressures and forces during transonic buffeting of a supercritical airfoil," *Journal of aircraft*, Vol. 21, No. 6, 1984, pp. 439–441.

[16] Jacquin, L., Molton, P., Deck, S., Maury, B., and Soulevant, D., "Experimental study of shock oscillation over a transonic supercritical profile," *AIAA journal*, Vol. 47, No. 9, 2009, pp. 1985–1994.

[17] Lee, B., "Oscillatory shock motion caused by transonic shock boundary-layer interaction," *AIAA journal*, Vol. 28, No. 5, 1990, pp. 942–944.

[18] Crouch, J., Garbaruk, A., Magidov, D., and Travin, A., "Origin of transonic buffet on aerofoils," *Journal of fluid mechanics*, Vol. 628, 2009, p. 357.

[19] Morgan, B., Duraisamy, K., Nguyen, N., Kawai, S., and Lele, S., "Flow physics and RANS modelling of oblique shock/turbulent boundary layer interaction," *Journal of Fluid Mechanics*, Vol. 729, 2013, p. 231.

[20] Cabot, W., and Moin, P., "Approximate wall boundary conditions in the large-eddy simulation of high Reynolds number flow," *Flow, Turbulence and Combustion*, Vol. 63, No. 1, 2000, pp. 269–291.

[21] Spalart, P. R., "Philosophies and fallacies in turbulence modeling," *Progress in Aerospace Sciences*, Vol. 74, 2015, pp. 1–15.

[22] Deck, S., "Numerical simulation of transonic buffet over a supercritical airfoil," *AIAA journal*, Vol. 43, No. 7, 2005, pp. 1556–1566.

[23] Grossi, F., Braza, M., and Hoarau, Y., "Prediction of transonic buffet by delayed detached-eddy simulation," *AIAA Journal*, Vol. 52, No. 10, 2014, pp. 2300–2312.

[24] Huang, J., Xiao, Z., Liu, J., and Fu, S., "Simulation of shock wave buffet and its suppression on an OAT15A supercritical airfoil by IDDES," *Science China Physics, Mechanics and Astronomy*, Vol. 55, No. 2, 2012, pp. 260–271.

[25] Housman, J. A., and Kiris, C. C., "Overset grid simulations for the second aiaa aeroelastic prediction workshop," *58th AIAA/ASCE/AHS/ASC Structures, Structural Dynamics, and Materials Conference*, 2017, p. 0640.

[26] Fukushima, Y., and Kawai, S., "Wall-modeled large-eddy simulation of transonic airfoil buffet at high Reynolds number," *AIAA Journal*, Vol. 56, No. 6, 2018, pp. 2372–2388.

[27] Kiris, C. C., Housman, J. A., Barad, M. F., Brehm, C., Sozer, E., and Moini-Yekta, S., "Computational framework for launch, ascent, and vehicle aerodynamics (LAVA)," *Aerospace Science and Technology*, Vol. 55, 2016, pp. 189–219.

[28] Housman, J. A., Stich, G.-D., Kocheemoolayil, J. G., and Kiris, C. C., "Predictions of Slat Noise from the 30P30N at High Angles of Attack using Zonal Hybrid RANS-LES," *25th AIAA/CEAS Aeroacoustics Conference*, 2019, p. 2438.

[29] Ghate, A. S., Housman, J. A., Stich, G.-D., Kenway, G., and Kiris, C. C., "Scale resolving simulations of the NASA Juncture Flow Model using the LAVA solver," *AIAA AVIATION 2020 FORUM*, 2020, p. 2735.

[30] Stich, G.-D., Housman, J. A., Kocheemoolayil, J. G., Kiris, C. C., and Bridges, J. E., "Large-Eddy Simulation of Jet Surface Interaction Noise," *25th AIAA/CEAS Aeroacoustics Conference*, 2019, p. 2475.

[31] Stich, G.-D., Housman, J. A., Ghate, A. S., and Kiris, C. C., "Jet Noise Prediction for Chevron Nozzle Flows withWall-Modeled Large-Eddy Simulation," *AIAA Scitech 2021 Forum*, 2021.

[32] Barad, M. F., Kocheemoolayil, J. G., and Kiris, C. C., "Lattice Boltzmann and Navier-Stokes Cartesian CFD Approaches for Airframe Noise Predictions," *23rd AIAA Computational Fluid Dynamics Conference*, 2017, p. 4404.

[33] Stich, D., Housman, J. A., Kocheemoolayil, J. G., Barad, M. F., Cadieux, F., and Kiris, C. C., "Application of Lattice Boltzmann and Navier-Stokes Methods to NASA's Wall Mounted Hump," *2018 Fluid Dynamics Conference*, 2018, p. 3855.

[34] Balakrishna, S., and Acheson, M., "Analysis of NASA common research model dynamic data," *49th AIAA Aerospace sciences meeting including the new horizons forum and aerospace exposition*, 2011, p. 1127.

[35] Musker, A., "Explicit expression for the smooth wall velocity distribution in a turbulent boundary layer," *AIAA Journal*, Vol. 17, No. 6, 1979, pp. 655–657.

[36] Bradshaw, P., "Compressible turbulent shear layers," *Annual Review of Fluid Mechanics*, Vol. 9, No. 1, 1977, pp. 33–52.

[37] Pirozzoli, S., Grasso, F., and Gatski, T., "Direct numerical simulation and analysis of a spatially evolving supersonic turbulent boundary layer at M= 2.25," *Physics of fluids*, Vol. 16, No. 3, 2004, pp. 530–545.

[38] Iyer, P. S., and Malik, M. R., "Analysis of the equilibrium wall model for high-speed turbulent flows," *Physical Review Fluids*, Vol. 4, No. 7, 2019, p. 074604.

[39] Bermejo-Moreno, I., Campo, L., Larsson, J., Bodart, J., Helmer, D., and Eaton, J., "Confinement effects in shock wave/turbulent boundary layer interactions through wall-modelled large-eddy simulations," *Journal of Fluid Mechanics*, Vol. 758, 2014, p. 5–62. doi:10.1017/jfm.2014.505.

[40] Larsson, J., Kawai, S., Bodart, J., and Bermejo-Moreno, I., "Large eddy simulation with modeled wall-stress: recent progress and future directions," *Mechanical Engineering Reviews*, Vol. 3, No. 1, 2016, pp. 15–00418.

[41] Bose, S. T., and Park, G. I., "Wall-modeled large-eddy simulation for complex turbulent flows," *Annual review of fluid mechanics*, Vol. 50, 2018, pp. 535–561.

[42] Caruelle, B., and Ducros, F., "Detached-eddy simulations of attached and detached boundary layers," *International Journal of Computational Fluid Dynamics*, Vol. 17, No. 6, 2003, pp. 433–451.

[43] Spalart, P. R., Deck, S., Shur, M. L., Squires, K. D., Strelets, M. K., and Travin, A., "A new version of detached-eddy simulation, resistant to ambiguous grid densities," *Theoretical and computational fluid dynamics*, Vol. 20, No. 3, 2006, p. 181.

[44] Deck, S., "Recent improvements in the zonal detached eddy simulation (ZDES) formulation," *Theoretical and Computational Fluid Dynamics*, Vol. 26, No. 6, 2012, pp. 523–550.

[45] Deck, S., and Renard, N., "Towards an enhanced protection of attached boundary layers in hybrid RANS/LES methods," *Journal of Computational Physics*, Vol. 400, 2020, p. 108970.

[46] Knopp, T., and Probst, A., "An algebraic sensor for the RANS-LES switch in delayed detached-eddy simulation," *New Results in Numerical and Experimental Fluid Mechanics VIII*, Springer, 2013, pp. 457–464.

[47] Ashton, N., "Recalibrating Delayed Detached-Eddy Simulation to eliminate modelled-stress depletion," *23rd AIAA Computational Fluid Dynamics Conference*, 2017, p. 4281.

[48] Jain, N., and Baeder, J. D., "Assessment of shielding parameters in conventional DDES method under the presence of alternative turbulence length scales," *23rd AIAA Computational Fluid Dynamics Conference*, 2017, p. 4282.

[49] Brehm, C., Barad, M. F., Housman, J. A., and Kiris, C. C., "A comparison of higher-order finite-difference shock capturing schemes," *Computers & Fluids*, Vol. 122, 2015, pp. 184–208.

[50] Shu, C.-W., "High order weighted essentially nonoscillatory schemes for convection dominated problems," *SIAM review*, Vol. 51, No. 1, 2009, pp. 82–126.

[51] Deng, X., and Zhang, H., "Developing high-order weighted compact nonlinear schemes," *Journal of Computational Physics*, Vol. 165, No. 1, 2000, pp. 22–44.

[52] Deng, X., Mao, M., Tu, G., Liu, H., and Zhang, H., "Geometric conservation law and applications to high-order finite difference schemes with stationary grids," *Journal of Computational Physics*, Vol. 230, No. 4, 2011, pp. 1100–1115.

[53] Harten, A., Lax, P. D., and Leer, B. v., "On upstream differencing and Godunov-type schemes for hyperbolic conservation laws," *SIAM review*, Vol. 25, No. 1, 1983, pp. 35–61.

[54] Deng, X., "New high-order hybrid cell-edge and cell-node weighted compact nonlinear schemes," *20th AIAA Computational Fluid Dynamics Conference*, 2011, p. 3857.

[55] Nonomura, T., and Fujii, K., "Robust explicit formulation of weighted compact nonlinear scheme," *Computers & Fluids*, Vol. 85, 2013, pp. 8–18.

[56] Thornber, B., Mosedale, A., Drikakis, D., Youngs, D., and Williams, R. J., "An improved reconstruction method for compressible flows with low Mach number features," *Journal of computational Physics*, Vol. 227, No. 10, 2008, pp. 4873–4894.

[57] Bridges, J., Henderson, B., and Huff, D., "Top-Mounted Propulsion Test Plans (TMP17)," 2017.

[58] Housman, J. A., and Kiris, C. C., "Slat Noise Predictions using Higher-Order Finite-Difference Methods on Overset Grids," *22nd AIAA/CEAS Aeroacoustics Conference*, 2016, p. 2963.

[59] Gottlieb, S., and Shu, C.-W., "Total variation diminishing Runge-Kutta schemes," *Mathematics of computation*, Vol. 67, No. 221, 1998, pp. 73–85.

[60] Vreman, A., "An eddy-viscosity subgrid-scale model for turbulent shear flow: Algebraic theory and applications," *Physics of fluids*, Vol. 16, No. 10, 2004, pp. 3670–3681.

[61] Ghate, A., Towne, A., and Lele, S., "Broadband reconstruction of inhomogeneous turbulence using spectral proper orthogonal decomposition and Gabor modes," *Journal of Fluid Mechanics*, Vol. 888, 2020.

[62] Ghate, A. S., and Lele, S. K., "Gabor mode enrichment in large eddy simulations of turbulent flow," *Journal of Fluid Mechanics*, Vol. 903, 2020, p. A13. doi:10.1017/jfm.2020.622.

[63] Spalart, P. R., "Strategies for turbulence modelling and simulations," *International Journal of Heat and Fluid Flow*, Vol. 21, No. 3, 2000, pp. 252–263.

[64] Menter, F., "Zonal two equation kw turbulence models for aerodynamic flows," *23rd fluid dynamics, plasmadynamics, and lasers conference*, 1993, p. 2906.

[65] Rivers, M. B., and Dittberner, A., "Experimental investigations of the NASA common research model," *Journal of Aircraft*, Vol. 51, No. 4, 2014, pp. 1183–1193.

[66] Rivers, M. B., Rudnik, R., and Quest, J., "Comparison of the NASA Common Research Model European Transonic Wind Tunnel Test Data to NASA Test Data," *53rd AIAA Aerospace Sciences Meeting*, 2015, p. 1093.

[67] Rivers, M., and Dittberner, A., "Experimental investigations of the nasa common research model in the nasa langley national transonic facility and nasa ames 11-ft transonic wind tunnel," *49th AIAA aerospace sciences meeting including the new horizons forum and aerospace exposition*, 2011, p. 1126.

[68] Keye, S., Brodersen, O., and Rivers, M. B., "Investigation of aeroelastic effects on the NASA common research model," *Journal of Aircraft*, Vol. 51, No. 4, 2014, pp. 1323–1330.